Photocurrents, inverse Faraday effect, and photospin Hall effect in Mn₂Au

Special Collection: Emerging Materials in Antiferromagnetic Spintronics

M. Merte ; F. Freimuth ; D. Go ; T. Adamantopoulos ; F. R. Lux ; L. Plucinski; O. Gomonay ;
S. Blügel ; Y. Mokrousov ✉

Check for updates

CrossMark

View Online

Export Citation

Photocurrents, inverse Faraday effect, and photospin Hall effect in Mn₂Au

View Online   Export Citation   CrossMark

M. Merte,[1,2,3,a] F. Freimuth,[1,3,b] D. Go,[1] T. Adamantopoulos,[1,2] F. R. Lux,[3] L. Plucinski,[1]
O. Gomonay,[3] S. Blügel,[1] and Y. Mokrousov[1,3,c]

AFFILIATIONS

[1] Peter Grünberg Institut and Institute for Advanced Simulation, Forschungszentrum Jülich and JARA, 52425 Jülich, Germany
[2] Department of Physics, RWTH Aachen University, 52056 Aachen, Germany
[3] Institute of Physics, Johannes Gutenberg University Mainz, 55099 Mainz, Germany

Note: This paper is part of the Special Topic on Emerging Materials in Antiferromagnetic Spintronics.
[a] Electronic mail: maximilian.merte@rwth-aachen.de
[b] Electronic mail: f.freimuth@fz-juelich.de
[c] Author to whom correspondence should be addressed: y.mokrousov@fz-juelich.de

ABSTRACT

Among antiferromagnetic materials, Mn₂Au is one of the most intensively studied, and it serves as a very popular platform for testing various ideas related to antiferromagnetic magnetotransport and dynamics. Since recently, this material has also attracted considerable interest in the context of optical properties and optically-driven antiferromagnetic switching. In this work, we use first principles methods to explore the physics of charge photocurrents, spin photocurrents, and the inverse Faraday effect in antiferromagnetic Mn₂Au. We predict the symmetry and magnitude of these effects and speculate that they can be used for tracking the dynamics of staggered moments during switching. Our calculations reveal the emergence of large photocurrents of spin in collinear Mn₂Au, whose properties can be understood as a result of a non-linear optical version of the spin Hall effect, which we refer to as the *photospin Hall effect*, encoded into the relation between the driving charge and resulting spin photocurrents. Moreover, we suggest that even a very small canting in Mn₂Au can give rise to colossal spin photocurrents that are *chiral* in flavor. We conclude that the combination of staggered magnetization with the structural and electronic properties of this material results in a unique blend of prominent photocurrents, which makes Mn₂Au a unique platform for advanced optospintronics applications.

I. INTRODUCTION

In recent years, antiferromagnets (AFMs) have attracted enormous interest in the context of spintronics applications due to a set of unique properties that make them often more favorable when compared to conventional ferromagnetic materials.[1–3] For example, random access memory devices based on antiferromagnetic materials have already been realized,[4] and THz switching of antiferromagnetic memory devices via current-induced spin-torques has been demonstrated.[4,5] However, in order to gain reliable control over antiferromagnetic THz dynamics, one has to move away from conventional electronics, which are not sufficiently fast for the purpose. To overcome this speed limitation, the concept of all optical

switching was proposed,[6–9] where switching and read-out are performed optically, often with THz laser sources. As a consequence, optical manipulation, and in particular the read-out of the Néel vector during optical dynamics in antiferromagnets, becomes a matter of grave importance.[10,11] In this context, the properties of optically generated photocurrents occupy a special place.[12–16]

Some of the major promises of antiferromagnetic spintronics hinge on our ability to get control over the properties and timescales of ultrafast antiferromagnetic dynamics triggered by optical excitations. In the context of antiferromagnetic spintronics, Mn₂Au has emerged as a very successful representative, as it can be easily fabricated, it allows for Néel type spin–orbit torques that are linear in the field and can be used to switch the staggered magnetization

in this material,[17–19] and it is a good metal with a very high Néel temperature, which is key for pronounced magnetotransport and magneto-optical response at room temperature. Owing to its relative structural and chemical simplicity, in the field of antiferromagnetism, Mn_2Au has long been a guinea pig for testing novel concepts relying on robust antiferromagnetic order and emergent functionalities. The optically driven dynamical properties of Mn_2Au have become a target of recent attention as well. For example, recently, an optical manipulation of magnetic order in Mn_2Au has been achieved by a combination of laser pulses and strain.[20,21] However, in order to move forward in pursuing optical implementations based on Mn_2Au, it is important to understand in detail the optical response of this material, in particular the behavior of photocurrents and the inverse Faraday effect (IFE), in relation to its electronic and magnetic structure.

In this work, we use the *ab-initio*-based Keldysh formalism, which we have applied in the past to various materials, to address the photo-response characteristics of bulk Mn_2Au. In particular, we study the microscopic origin, symmetry, and magnitude of charge photocurrents in this material as a function of laser frequency, light polarization, band filling, degree of disorder, and Néel vector direction. We identify qualitatively different types of photocurrents and demonstrate that by carefully measuring the evolution of photocurrents, it is possible to track the optical magnetization dynamics of Mn_2Au. We also predict the magnitude and properties of the uniform and staggered laser-induced spin polarization, i.e., the inverse Faraday effect. In addition, by considering the laser-generated currents of spin, we introduce the notion of a *photospin Hall effect* and a photospin Hall angle, which characterize the ratio between the transverse photo-induced currents of charge and spin. Finally, we demonstrate that breaking the symmetry in the system even by a small canting of staggered moments unleashes colossal *chiral spin photocurrents* whose sign can be controlled by the sense of canting. Overall, we provide an important qualitative and quantitative understanding of photo-induced phenomena in Mn_2Au, which may prove vital not only for further integration of this material into the optical realm but generally for engineering the optical properties of wider classes of antiferromagnets.

The article is structured as follows. In Sec. II, we outline the assumed electronic structure and use computational methods. Section III B discusses the dependence of charge photocurrents on the Néel vector orientation, while in Sec. III C, properties of charge photocurrents are discussed for a fixed Néel vector orientation along the magnetic easy axis. In Sec. IV, we analyze the inverse Faraday effect and report a large staggered response on the Mn sublattices. Section V discusses laser induced spin currents with a proposed photospin Hall effect in Sec. V C. In Sec. VI, we analyze the effect of canting. Section VI A discusses the emergence of chiral photocurrents in the canted scenario. In close analogy, we report on large chiral spin photocurrents driven by the chiral inverse Faraday effect in Sec. VI B. The manuscript ends with conclusions.

II. ELECTRONIC STRUCTURE AND COMPUTATIONAL DETAILS

The spatial inversion symmetry $\mathscr{P}$ is broken in Mn_2Au by the staggered magnetic moments on the Mn sublattices [see Figs. 1(a) and 1(b)], and thus only magnetic photocurrents are expected to survive. These are expected to strongly depend on the orientation and strength of the magnetic moments. On the other hand, Mn_2Au possesses a combination of spatial inversion $\mathscr{P}$ with a time reversal operation $\mathscr{T}$, known as $\mathscr{PT}$-symmetry. The characteristic $\mathscr{PT}$-symmetry of Mn_2Au is expected to suppress extrinsic contributions like the side-jump and skew-scattering contributions[22] making Mn_2Au the ideal candidate to study the properties of pure magnetic photocurrents.

Mn_2Au has a tetragonal unit cell with space group $I4/mmm$[23] [see Fig. 1(a)]. The experimental lattice constants $a = 6.291$ a.u. and $c = 16.142$ a.u. were assumed for the calculations.[23] The magnetization in the two Mn layers along the z-axis has collinear antiferromagnetic ordering[24] and is assumed to be along the easy [110] direction unless specified otherwise. In Fig. 1(a), we show the assumed structure. Electronic structure calculations were performed with the full-potential linearized augmented plane-wave code FLEUR.[25] For self-consistent calculations, we used a plane-wave cutoff of 4.0 a.u.$^{-1}$ and a total of 1728 k-points in the three-dimensional Brillouin zone (BZ). The plane wave cutoffs for the potential (g_{max}) and exchange-correlation potential ($g_{max,xc}$) were set to 12.0 and 12.0 a.u.$^{-1}$, respectively. The muffin-tin radii for Mn and Au atoms were set to 2.53 and 2.60 a.u., respectively. The nonrelativistic Perdew–Burke–Ernzerhof (PBE)[26] exchange-correlation functional was used. The spin–orbit coupling was included in the second variation.

To reduce the numerical effort, the size of the basis set was decreased by half by using a reduced representation of the unit cell containing only three atoms, as shown in Fig. 1(b). For the initial projections of the maximally localized Wannier functions (MLWFs),[27] s-, p-, and d-orbitals were used for both Mn and Au atoms resulting in 54 Wannier functions for the case with three atoms in the unit cell. In Fig. 1(c), we show the computed *ab initio* bands in cyan and magenta for the spin up and down states, respectively, while Wannier-interpolated bands are plotted in black. Within the frozen energy window, set to 13.6 eV, which is 4.2 eV above the true Fermi level, the interpolation shows a negligible deviation from the *ab initio* band structure, which allows us to perform simulations of optical effects with frequencies up to $\hbar\omega = 4.2$ eV when evaluated at the true Fermi level. The electronic structure of Mn_2Au is manifestly metallic in nature. The density of states (DOS) for spin up (left) and spin down (right) states is shown in Fig. 1(c). In the relevant energy region for optical transitions of about 4 eV around the Fermi level, the largest contribution to the DOS comes from the interstitial region, with a similarly large contribution from the Mn atoms. The states of Au dominate the DOS only deeper into the valence bands (below −4 eV). The DOS exhibits a large peak at +1.2 eV above the Fermi level and a group of similar peaks between −1.6 and −3.2 eV. The two Mn DOS (red and blue) undergo a visible spin flip when crossing from the group of peaks below the Fermi level to the region above it. The corresponding accumulation of states in these regions of energy may be associated with regions of pronounced response in some of the cases, as discussed further.

In our work, we investigate second-order optical effects: charge and spin photocurrents, as well as non-equilibrium optically-induced spin density, known as the inverse Faraday effect.[7,28–30] Namely, we calculate the spin accumulation, charge, and spin photocurrents that arise at second order in the perturbing electric field of a continuous laser pulse of frequency ω by using the expressions
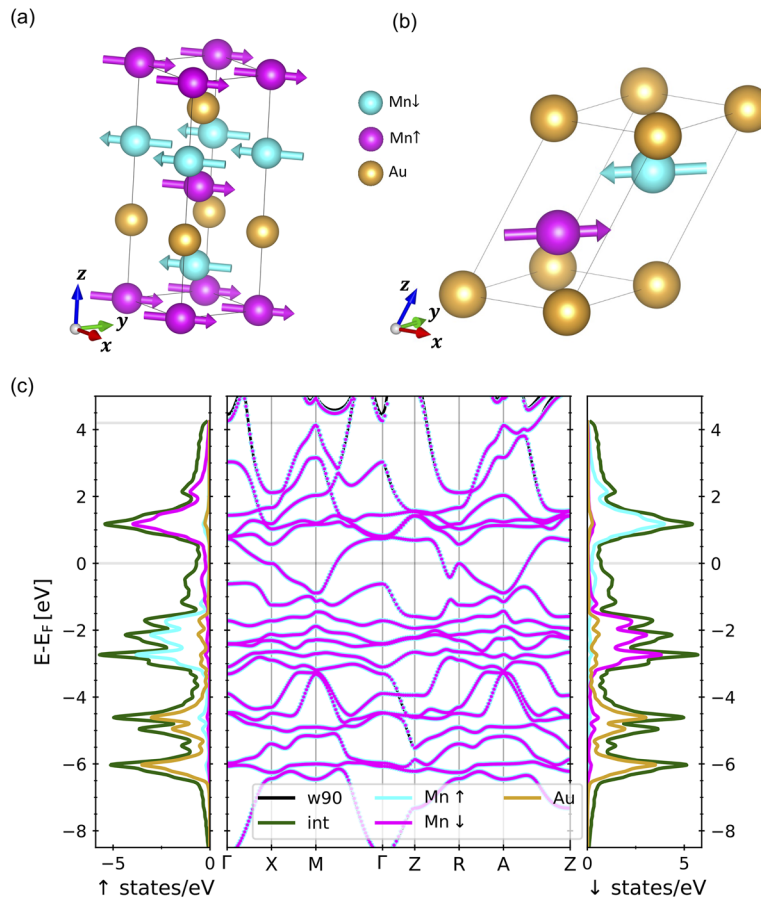
(a)

(b)

Mn↓
Mn↑
Au

(c)

FIG. 1. The unit cell of Mn$_2$Au with staggered magnetization along the [110] direction. Cyan and magenta balls indicate Mn atoms with arrows depicting the magnetic moments. Golden balls represent Au atoms. (a) Regular tetragonal unit cell hosting six atoms. (b) Reduced unit cell with three atoms. (c) Electronic properties of Mn$_2$Au with staggered magnetization along the [110]-direction. The left panel shows the *ab initio* density of states (DOS) of spin down states decomposed into contributions from the interstitial region (green curve) and individual atomic sites Mn↑, Mn↓, and Au (cyan, magenta, and golden curves). The right hand panel shows the DOS of the spin up states. In the center panel of (c), the *ab initio* bandstructure (cyan and magenta dots for spin-up and spin-down states) is compared with the Wannier-interpolated bandstructure (black curve).

that were previously derived by us in Ref. 30 within the framework of the Keldysh formalism, and applied to various systems.[31–33]

Within our approach, the electric field is modeled as a coherent wave of the kind

$$E(t) = -\frac{\partial A(t)}{\partial t} = \text{Re}\big[E_0 \boldsymbol{\epsilon} e^{-i\omega t}\big], \qquad (1)$$

where E_0 is the real valued field strength, $\boldsymbol{\epsilon}$ its polarization vector, ω the frequency, and $A(t)$ is the vector potential. In our work, a circularly polarized pulse propagating, for example, in the z direction is described by $\boldsymbol{\epsilon} = (1, \lambda i, 0)/\sqrt{2}$, where $\lambda = \pm 1$ is the helicity. Linearly polarized light along, for example x or y axes is described by $\boldsymbol{\epsilon} = (1, 0, 0)$ and $\boldsymbol{\epsilon} = (0, 1, 0)$, respectively, while generalization to arbitrary axes is obvious. The corresponding perturbation of the Hamiltonian reads:[30]

$$\delta H(t) = e\boldsymbol{v} \cdot A(t), \qquad (2)$$

where $\boldsymbol{v}$ is the velocity operator. To model the photocurrent **J** associated with the second order current response to the electric field,[34–37] we use the Keldysh non-equilibrium Green function technique, wherein expectation values can be calculated by coupling their associated operator to the lesser Green's function $G^<$.[38] For example, a current **J** is obtained by coupling the velocity operator $\boldsymbol{v}$ to the lesser Green's function $G^<$,[39]

$$\mathbf{J} = \frac{\hbar}{2i} \text{Tr}\big[\boldsymbol{v}G^<\big]. \qquad (3)$$

To obtain the lesser Green's function $G^<$ of the nonequilibrium system relevant for the calculation of various photogalvanic effects, we plug the perturbation of Eq. (2) into the Dyson equation on the Keldysh contour[38] and iteratively evaluate it up to terms quadratic in $\delta H(t)$. A full expression of the resulting nonequilibrium lesser Green's function can be found in Appendix A of Ref. 30. Combining the second order lesser Green's function $G_2^<$ of

Ref. 30 with Eq. (3) yields an expression for the second order photocurrent density (which we refer as the current for shortness of notation),[39]

$$J_i = \frac{a_0^2 eI}{\hbar c}\left(\frac{E_H}{\hbar\omega}\right)^2 \mathrm{Im}\sum_{jk}\varepsilon_j\varepsilon_k^*\,\varphi_{ijk}, \qquad (4)$$

where a_0 is the Bohr radius, $E_H = e^2/(4\pi\varepsilon_0 a_0)$ is the Hartree energy, e is the elementary charge, $\hbar$ is the reduced Planck constant, and I is

the field intensity. The field intensity is given by $I = \varepsilon_0 c E_0^2/2$, where ε_0 is the vacuum permittivity and c is the speed of light. Throughout this work, the assumed intensity of the pulse was set to 10 GW/cm², which corresponds to typical values of the fluence of the order of 0.5 mJ/cm² for a 50 fs laser pulse.[40] Since the laser intensity enters the formalism only as a prefactor [see Eq. (4)], the results can be easily converted to other intensity values. The quantity φ_{ijk}, to which we refer below as the second order conductivity tensor, is defined as[39]

$$\begin{aligned}
\varphi_{ijk} = \frac{2}{a_0 E_H}\int\frac{d^3k}{(2\pi)^3}\int dE\,\mathrm{Tr}\big[&f(E)v_i G_{\boldsymbol{k}}^R(E)v_j G_{\boldsymbol{k}}^R(E-\hbar\omega)v_k G_{\boldsymbol{k}}^R(E) - f(E)v_i G_{\boldsymbol{k}}^R(E)v_j G_{\boldsymbol{k}}^R(E-\hbar\omega)v_k G_{\boldsymbol{k}}^A(E)\\
&+ f(E)v_i G_{\boldsymbol{k}}^R(E)v_k G_{\boldsymbol{k}}^R(E+\hbar\omega)v_j G_{\boldsymbol{k}}^R(E) - f(E)v_i G_{\boldsymbol{k}}^R(E)v_k G_{\boldsymbol{k}}^R(E+\hbar\omega)v_j G_{\boldsymbol{k}}^A(E)\\
&+ f(E-\hbar\omega)v_i G_{\boldsymbol{k}}^R(E)v_j G_{\boldsymbol{k}}^R(E-\hbar\omega)v_k G_{\boldsymbol{k}}^A(E) + f(E+\hbar\omega)v_i G_{\boldsymbol{k}}^R(E)v_k G_{\boldsymbol{k}}^R(E+\hbar\omega)v_j G_{\boldsymbol{k}}^A(E)\big],
\end{aligned} \qquad (5)$$

where v_i is the i-th component of the velocity operator, $f(E)$ is the Fermi–Dirac distribution function, and $G_{\boldsymbol{k}}^{R/A}$ is the equilibrium retarded advanced Green's function, respectively. In order to describe the effect of disorder in the electronic states on the computed quantities, the method of constant lifetime broadening Γ, naturally included in Keldysh formalism, was used,[41]

$$G_{\boldsymbol{k}}^R(E) = \hbar\sum_n\frac{|\boldsymbol{k}n\rangle\langle\boldsymbol{k}n|}{E - E_{\boldsymbol{k}n} + i\Gamma}. \qquad (6)$$

The advanced Green's function is defined as a complex conjugate of the retarded Green's function $G_{\boldsymbol{k}}^A(E) = [G_{\boldsymbol{k}}^R(E)]^\dagger$. A 256 × 256×256 k-mesh has proven to be sufficient to obtain the convergent results of Eq. (5) throughout the article.

As discussed, e.g., by Ibañez-Azpiroz *et al.*,[37] we introduce the photoconductivity tensor σ_{ijk} such that the photocurrent in Eq. (4) is given by $J_i = \mathrm{Re}\sum_{jk}2\sigma_{ijk}E_j E_k^*$, similarly to the definition of Eq. (7) in Ref. 37. By inserting[30] the laser intensity $I = \varepsilon_0 c E_0^2/2$ into Eq. (4), consequently, $\sigma_{ijk} = i\frac{a_0^2 e\varepsilon_0}{2\hbar}\frac{\varphi_{ijk}}{2}$, where φ_{ijk} is the tensor defined in Eq. (5). The expression for the spin photocurrent Q_i^s flowing in the direction i with spin polarization along axis s is obtained by replacing the velocity operators v_i in Eq. (5) with the operator of the spin velocity $\{v_i, \tau_s\}$, where τ_s is one of the Pauli matrices. To obtain Q_i^s, the prefactor $a_0^2 eI/\hbar c$ in Eq. (4) is replaced with the prefactor $-a_0^2 I/4c$. For quantifying the inverse Faraday effect, the expression for the photo-induced spin density δS_i is obtained by replacing the velocity operators v_i in Eq. (5) with the operator of (local) spin; the prefactor $a_0^2 eI/\hbar c$ in (4) is replaced with $-\hbar\, a_0^3 I/2c$.

III. PHOTOCURRENTS OF CHARGE

First, we focus on the properties of the photocurrents of charge in Mn₂Au. We start by discussing the dependence of the photocurrent on the orientation of the Néel vector within the xy-plane, then

fix the Néel vector to the [110]-direction, and after the analyzing symmetry properties of the k-resolved photocurrents, proceed with the discussion of the spectral properties of the photocurrents. We conclude our discussion by analyzing the influence of lifetime broadening and identifying magnetic photocurrents by considering the broadening values of the positive and negative signs. For the sake of simplicity, below we will refer to currents arising in response to linearly and circularly polarized light as *linear* and *circular*, respectively. This should not be confusing, keeping in mind that both types of responses we compute are manifestly second order in the applied field.

A. Symmetry analysis

In order to determine which components of a response matrix are allowed by symmetry, one usually first determines if the response coefficients transform like an axial or polar tensor. Next, one uses Neumann's principle in order to find out which tensor components are allowed by symmetry. The classification of response matrices into axial or polar categories is often sufficient, in particular for normal metals and ferromagnets. However, in antiferromagnets, these two categories may be insufficient. Therefore, in Ref. 42, we explain that the response coefficients in antiferromagnets can be discussed in terms of axial (a), polar (p), staggered axial (sa), and staggered polar (sp) tensors.

In the collinear scenario, Mn₂Au can host various photocurrents that are of first order in the Néel vector N,

$$J_i = \chi_{ijkl}^{(4sa)}E_j E_k^* N_l, \qquad (7)$$

where $\chi_{ijkl}^{(4sa)}$ is a staggered axial tensor of rank 4. We find that 10 staggered axial tensors of rank 4 are allowed by symmetry in Mn₂Au. We list them in Table I, where we employ the notation

$$\delta_{nopq}^{(ijkl)} = \delta_{in}\delta_{jo}\delta_{kp}\delta_{lq} = \langle ijkl\rangle. \qquad (8)$$

TABLE I. List of staggered axial tensors of rank 4 allowed by symmetry in Mn$_2$Au. The notation introduced in Eq. (8) is used. $\parallel$ and $\perp$ refer to Néel vector directions in-plane and out-of-plane, respectively.

No.	$\chi_{ijkl}^{(4sa)}$		No.	$\chi_{ijkl}^{(4sa)}$	
1	$\langle 3321\rangle - \langle 3312\rangle$	$\parallel$	6	$\langle 3213\rangle - \langle 3123\rangle$	$\perp$
2	$\langle 1121\rangle - \langle 2212\rangle$	$\parallel$	7	$\langle 2313\rangle - \langle 1323\rangle$	$\perp$
3	$\langle 1211\rangle - \langle 2122\rangle$	$\parallel$	8	$\langle 2133\rangle - \langle 1233\rangle$	$\perp$
4	$\langle 3231\rangle - \langle 3132\rangle$	$\parallel$	9	$\langle 2221\rangle - \langle 1112\rangle$	$\parallel$
5	$\langle 2331\rangle - \langle 1332\rangle$	$\parallel$	10	$\langle 2111\rangle - \langle 1222\rangle$	$\parallel$

B. Néel vector dependence of the charge photocurrents

Since the inversion symmetry $\mathscr{P}$ in Mn$_2$Au is broken only by the magnetization on the Mn sublattices and not the crystal structure itself, the resulting photocurrents are expected to be of purely magnetic origin. The orientation of the magnetic photocurrent is thus expected to depend directly on the orientation of the Néel vector. Indeed, in a recent experiment, the magnetic linear dichroism was found to have a distinct dependence on the relative orientation of the linearly polarized light and the Néel vector.[20] Furthermore, the nonlinear anomalous Hall effect (AHE) was recently proposed to measure the Néel vector orientation.[43]

We first compute the photocurrents J_x and J_y for the Néel vector lying in the (001)-plane along the x- and y-directions for the frequency of linearly polarized light of 1.55 eV and a lifetime of 100 meV. We find that in the case of the Néel vector aligned along x, the J_y component shows the largest response of almost 90×10^{10} A/m^2 when the polarization is along y, while for the light polarized along x, the current response switches signs and is reduced in amplitude to $\sim 70 \times 10^{10}$ A/m^2. The J_y component in response to light linearly polarized along the x and y-directions corresponds to symmetry tensors Nos. 9 and 10 in Table I, respectively. The J_y component in response to light linearly polarized along z is given by symmetry tensor No. 5. The J_x component in response to light rotating in the xy-plane corresponds to tensor No. 2. Table I suggests that the situation is reversed when the Néel vector is instead aligned along the y-direction. As a result, the overall angular dependence with respect to the plane of light polarization is shifted by 90° between the two Néel vector orientations with an additional sign reversal of the resulting current, yielding

$$J_y(\mathbf{N}\|x; \boldsymbol{\varepsilon}\|y) = -J_x(\mathbf{N}\|y; \boldsymbol{\varepsilon}\|x),$$
$$J_y(\mathbf{N}\|x; \boldsymbol{\varepsilon}\|x) = -J_x(\mathbf{N}\|y; \boldsymbol{\varepsilon}\|y). \tag{9}$$

The fact that this symmetry property is generic is confirmed by calculations of the band filling dependence of the photocurrents, shown in Fig. 2 for linearly and circularly polarized light of $\hbar\omega = 1.55$ eV and $\Gamma = 100$ meV for $\mathbf{N}$ along x [left column, (a)] and $\mathbf{N}$ along y [right column, (b)]. In both scenarios, the largest photocurrent is flowing perpendicular to the staggered magnetization, while the photocurrent parallel to $\mathbf{N}$ is an order of magnitude smaller. The perpendicular current is maximized for linearly polarized light, while the parallel response is only driven by circularly polarized light. For the current perpendicular to the Néel vector, the finite response to circularly polarized light is sizable; however,

it remains helicity-independent and is shaped by responses to linearly polarized light. This indicates that the circular responses are just the averages of the linear responses spanning the plane normal to the direction of incidence of circularly-polarized light (e.g., the light blue curve in Fig. 2 is an average between the red and the yellow curves). This behavior is characteristic of the *magnetic linear photogalvanic effect* (magnetic LPGE), while the circular responses can be interpreted as the *magnetic circular photogalvanic effect* (magnetic CPGE). The data presented in Fig. 2 shows that the correspondence between the two scenarios is universal over the entire energy range.

C. Photocurrents for Néel vector along the easy axis

Here, we study the photocurrents for the case of $\mathbf{N}$ along the easy [110] direction.[44] For this case, the symmetry tensors of the system are given by combinations of the symmetry tensors from Table I for the scenarios of the Néel vector along the x- and y-directions. For example, currents in the xy-plane in response to linearly polarized light will be given by combinations of tensors Nos. 5, 9, and 10. From now on until the end of the chapter, for brevity, the responses will be discussed in terms of their projection onto $\mathbf{N}$ as $\|\mathbf{N}$, and as $\perp\mathbf{N}$ marking the projection onto the [1$\bar{1}$0] direction. Since the [110] and [100] directions are the easy axes and the z-direction is the hard axis,[44] we will refer to components within the xy-plane as "in-plane (IP)" and z-components as "out of plane (OOP)" responses. The laser field polarization $\boldsymbol{\varepsilon}$ will be projected onto these directions as well, with linear polarized fields denoted by $\boldsymbol{\varepsilon}\|\mathbf{N}$, $\boldsymbol{\varepsilon}\perp\mathbf{N}$ and $\boldsymbol{\varepsilon}\|z$. For circular polarized light rotating in the xy-plane, we use $\boldsymbol{\varepsilon}\circlearrowleft\lambda_x^y$ for counter- and $\boldsymbol{\varepsilon}\circlearrowright\lambda_x^y$ for clockwise rotation. Besides light rotating within the magnetic easy plane, we also consider circular polarized fields rotating in the plane spanned by z with the two in-plane directions $\|\mathbf{N}$ and $\perp\mathbf{N}$, which will be denoted by $\boldsymbol{\varepsilon}\circlearrowleft/\circlearrowright\lambda_{\|\mathbf{N}}^z$ and $\boldsymbol{\varepsilon}\circlearrowleft/\circlearrowright\lambda_{\perp\mathbf{N}}^z$.

1. Band-resolved contributions

Before proceeding with a detailed analysis of the behavior of the integrated photocurrents, we would like to get an impression of the "internal" band-resolved and k-resolved constituents of these integrated quantities. We start by scrutinizing the role of so-called *resonant transitions*,[33] i.e., contributions to the photocurrents that involve only two distinct band transitions, as opposed to a more general case where three distinct band transitions are involved (i.e., non-resonant transitions). The resonant transitions can be seen as transitions where the initial and final states are the same. It is known that the LPGE is given by such resonant transitions, while the CPGE effects can only be described by non-resonant transitions.[45,46] Indeed, as we have checked by explicit calculations, the magnetic LPGE currents $J_{\perp\mathbf{N}}$ discussed below are solely given by resonant transitions, while the magnetic CPGE currents $J_{\|\mathbf{N}}$ and J_z originate solely in non-resonant transitions.

The resonant transitions can be naturally presented and discussed in a band-resolved manner in the reciprocal space.[33] In Fig. 3, we show the parallel and perpendicular photocurrents, given by resonant transitions, arising in response to blue $\hbar\omega = 3.0$ eV light for linear polarization parallel and perpendicular to the Néel vector. As discussed earlier, the parallel component of the photocurrent integrates to zero over the Brillouin zone (BZ), with the perpendicular
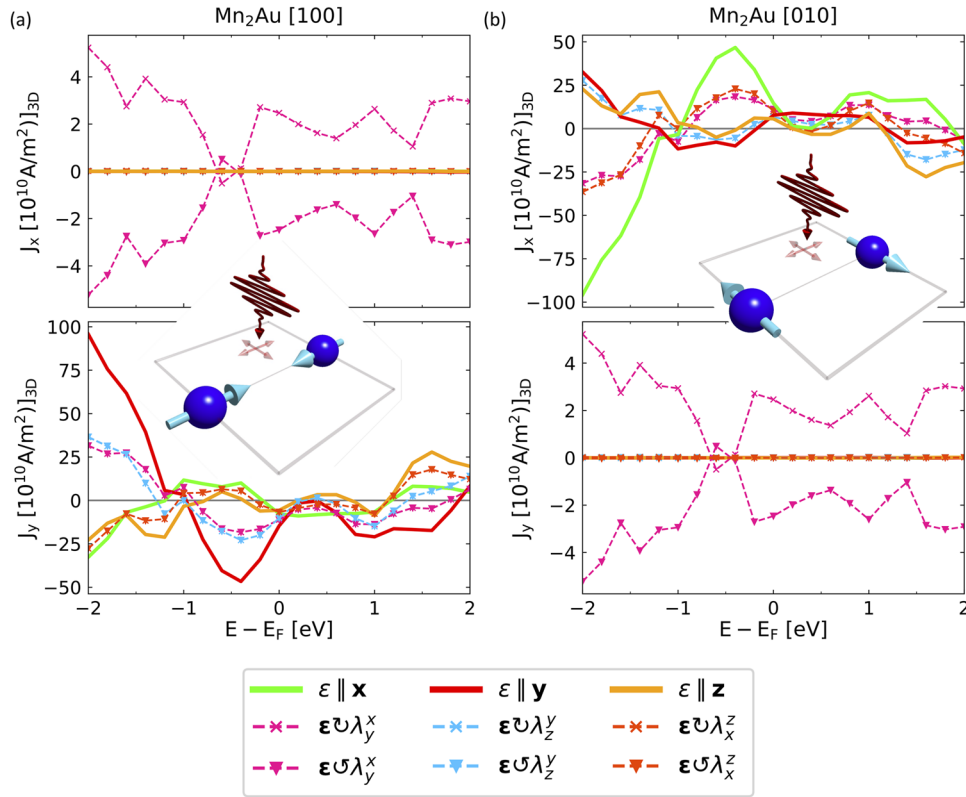
FIG. 2. J_x and J_y components of the charge photocurrent in Mn$_2$Au for the direction of the Néel vector along x (a) and y (b), in response to red laser light with $\hbar\omega = 1.55$ eV as a function of band filling. The broadening was set to $\Gamma = 100$ meV.

component being dominant. However, large resonant contributions are visible not only in the perpendicular scenario, shown in Fig. 3(b), but also in the case of the parallel component, shown in Fig. 3(a).

Let us first compare the two scenarios for light polarized along the Néel vector, $\boldsymbol{\varepsilon}\|\mathbf{N}$ (upper panel of Fig. 3). Clearly, at a given k-point, electronic transitions occur between bands that are separated by a frequency of 3.0 eV. For example, a prominent transition takes place between X and M points from -0.3 to $+2.7$ eV, visible both in (a) and (b). In the case of nonvanishing perpendicular current, both energy regions contribute positive values, while in the case of parallel current, the conduction and valence bands provide a response that is opposite in sign. In other regions of the BZ, both currents are very similar in strength and sign (see, for example, the transition along ΓX or ZR). Along RA, the transitions are of comparable strength but of the opposite sign between two cases. The regions from M to Γ and from A to Z host much more pronounced contributions to $J_{\|\mathbf{N}}$.

In the case of linearly polarized light with polarization perpendicular to the Néel vector (lower panel of Fig. 3), the distribution of significantly contributing transitions is notably different. Especially the transitions taking place along the ZRA are dominant. Another prominent contribution is visible along MΓ for both components

of the current. However, overall, the transitions ignited by linearly polarized light are visible along the high symmetry lines for both cases of $J_{\|\mathbf{N}}$ and $J_{\perp\mathbf{N}}$, often at the same k-points with only a difference in the sign and strength of the transition. Transitions do take place in the case of the symmetry-suppressed response $J_{\|\mathbf{N}}$, which suggests that they are canceled by transitions of the opposite sign in other regions of the BZ.

To get a better impression of the distribution of resonant transitions in the BZ, we analyze the distribution of the photocurrents in three slices of the BZ, which are parallel to the (001)-plane at $k_z = 0$ and $k_z = \pm 0.25$ in relative units (see Fig. 4), which shows the parallel (left column) and perpendicular (right column) photocurrents as contour plots over these slices. In the case of the overall nonvanishing $J_{\perp\mathbf{N}}$, the distribution of transitions has perfect mirror symmetry between the $+k_z^0$ and $-k_z^0$ slices (see right part of Fig. 4). For $J_{\|\mathbf{N}}$, on the other hand, the transitions are not only mirrored, but they also change sign as we change the slice from that at $+k_z^0$ to that at $-k_z^0$, thus integrating to zero over the entire BZ. The observation that while the integrated response is vanishing, the local contributions are pronounced suggests the possibility that the k-contributions can promote an integral response to linearly polarized light in $J_{\|\mathbf{N}}$ upon strain, canting (discussed further), or by going to third-order in the field responses.
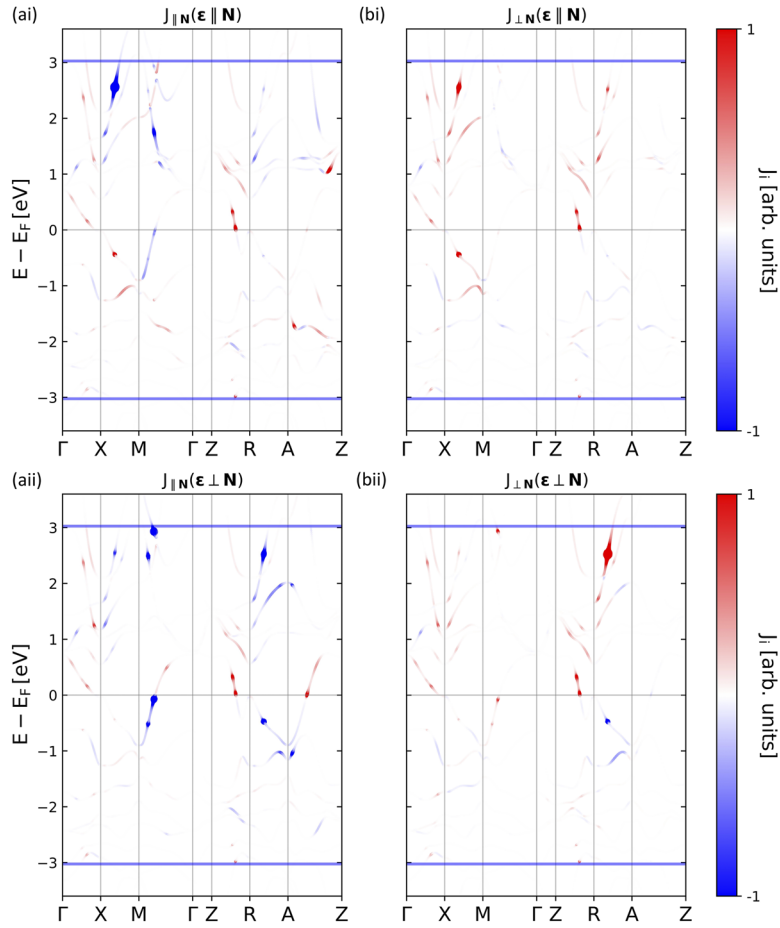
FIG. 3. Resonant band contributions to the photocurrents plotted along high symmetry lines in the Brillouin zone for the scenario of the Néel vector along [110]. The left column shows the photocurrent flowing parallel to the Néel vector in response to (ai) light linearly polarized along the Néel vector $J_{\parallel N}(\varepsilon \parallel \mathbf{N})$ and (aii) perpendicular to the Néel vector $J_{\parallel N}(\varepsilon \perp \mathbf{N})$. The right column shows the photocurrent flowing perpendicular to the Néel vector in response to linear polarized light (bi) along the Néel vector $J_{\perp N}(\varepsilon \parallel \mathbf{N})$ and (bii) perpendicular to the Néel vector $J_{\perp N}(\varepsilon \perp \mathbf{N})$. Here, the laser frequency is $\hbar\omega = 3.0$ eV, $\Gamma = 25$ meV, the true Fermi level is indicated by the horizontal gray line, and the edges of the selected energy interval $[E_F - \hbar\omega, E_F + \hbar\omega]$ are indicated by blue lines. The strength of the response at a given k-point is indicated by the band thickness and color.

2. Frequency and band filling dependence

We next study the frequency dependence of $J_{\perp N}$ currents. In order to compare the strength of the photocurrents to the values available in the literature, it is convenient to refer to the conductivity tensor as defined in Sec. II. We further project the conductivity tensor onto the $[1\bar{1}0]$-direction via $\sigma_{\perp N jk} = (\sigma_{xjk} - \sigma_{yjk})/\sqrt{2}$ and use the following rules:

$$\sigma_{\perp N}(\varepsilon \parallel \mathbf{N}) := \frac{1}{2}(\sigma_{\perp N xx} + \sigma_{\perp N yy}) + \frac{1}{2}(\sigma_{\perp N xy} + \sigma_{\perp N yx}),$$

$$\sigma_{\perp N}(\varepsilon \perp \mathbf{N}) := \frac{1}{2}(\sigma_{\perp N xx} + \sigma_{\perp N yy}) - \frac{1}{2}(\sigma_{\perp N xy} + \sigma_{\perp N yx}), \qquad (10)$$

$$\sigma_{\perp N}(\varepsilon \parallel \mathbf{z}) := \sigma_{\perp N zz},$$

so as to bring the conductivity into a shape compatible with the sense of linear polarization of the light.

In Fig. 5(a), we present the frequency dependence of the conductivity tensor as defined in Eq. (10) for different linear polarizations. We observe sizable values of photoconductivity for all polarization flavors across the complete presented frequency range of $\hbar\omega \in [0.20, 3.10]$ eV. For laser frequencies below $\hbar\omega = 1$ eV, the conductivity is negative in all cases. At $\hbar\omega = 0.8$ eV, the conductivity exhibits a peak of about -150 μA/V^2, similar in magnitude for all polarizations. Another peak of about $+100$ μA/V^2 is present at $\hbar\omega = 1.20$ eV if the laser light is linearly polarized within the xy-plane, while at the same time, the z-linear conductivity (orange line) shows a much smaller peak at this frequency. These conductivity values are comparable to those reported in the literature; e.g., Ibañez-Azpiroz et al.[37] reported a maximum conductivity of $\sim$40 μA/V^2 for the bulk semiconductor GaAs, and more recently, Zhang et al.[46] predicted a photoconductivity of almost 200 μA/V^2 in the two-dimensional van-der-Waals antiferromagnet CrI$_3$.
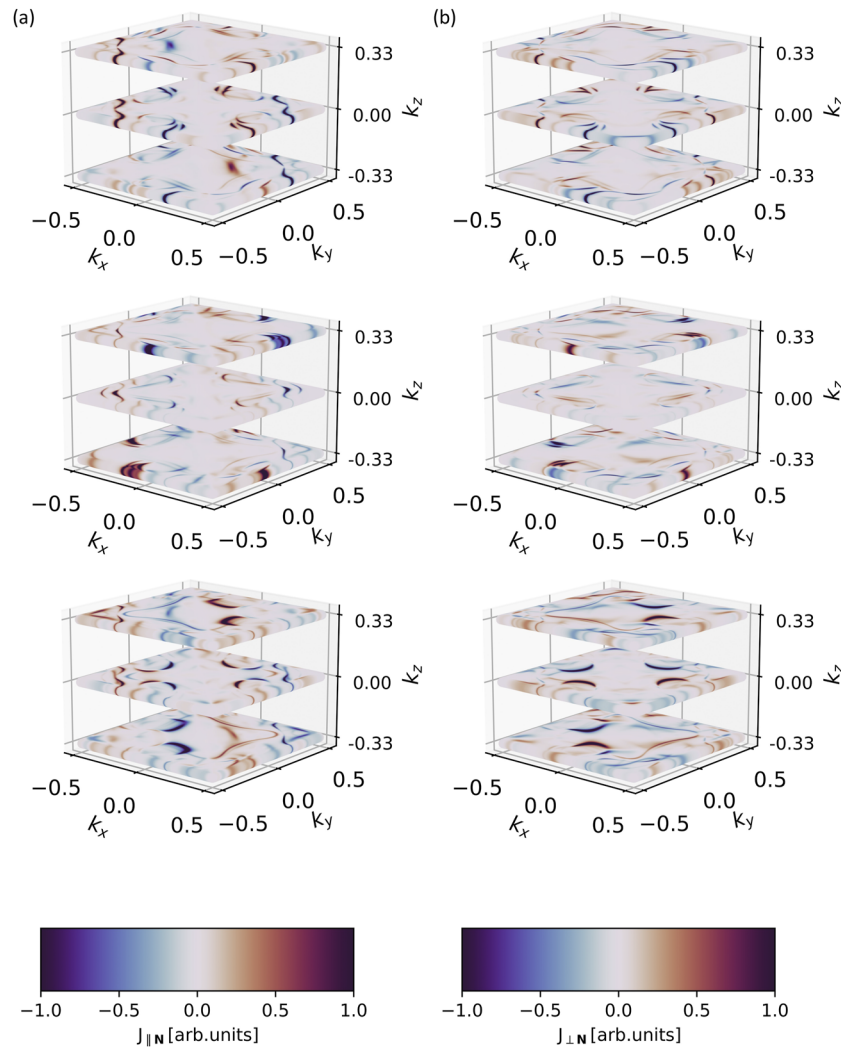
FIG. 4. Photocurrents resolved in the Brillouin zone for blue laser light of $\hbar\omega$ = 3.0 eV at Γ = 25 meV in different k_z-layers. The left column shows the parallel photocurrent $J_{\parallel N}$, and the right column shows the perpendicular photocurrent $J_{\perp N}$. The columns show different orientations of the linearly polarized light: in the first column, light is polarized along the Néel vector $\varepsilon \parallel N$; in the second column, light is polarized in the (001) plane but perpendicular to the Néel vector $\varepsilon \perp N$; and in the third column, light is polarized linearly along $\varepsilon \parallel z$.

In the range of $\hbar\omega$ = 1.20 eV up to about $\hbar\omega$ = 2.00 eV, the conductivity is positive for all polarizations. At $\hbar\omega$ = 2.00 eV, the two in-plane-polarized conductivities (blue and red lines) are suppressed and start to oscillate with frequency up to 3.1 eV, remaining predominantly opposite in sign. This may prove useful; indeed, for example, the conductivity $\sigma_{\perp N}$ can be switched in sign between identical magnitude values of ± 25 $\mu A/V^2$ at a laser frequency of $\hbar\omega$ = 3.00 eV by simply rotating the linear polarization vector by 90° in the xy-plane. Owing to the conveniently opposite sign of the two in-plane polarized responses at $\hbar\omega$ = 3.00, this frequency will be used as the default for the remaining discussion.

By staying at $\hbar\omega$ = 3.00 eV in Fig. 5(b), we present the dependence of $J_{\perp N}$ on band filling. As discussed earlier, the circular responses (symbols) are helicity-independent and are determined by an average of the two linear responses spanning the plane of rotation of the pulse. Data shown in Fig. 5(b) reveal that the aforementioned opposite sign between $J_{\perp N}$ driven by light with $\varepsilon \parallel N$ and $\varepsilon \perp N$ (red and blue lines) is robust with respect to the band filling for a range of almost 2 eV around the true Fermi level. At about 0.5 eV below the true Fermi level, the photocurrents for two in-plane linear polarizations have identical magnitude and opposite sign; this can be directly seen from the vanishing response to circularly polarized light rotating in the plane of the Néel vector (pink symbols), which vanishes there as a result of being an average over two currents of opposite sign. Notably, the band filling behavior is manifestly different from that exhibited by the photocurrents at another frequency and band smearing, shown in Fig. 2, and we will scrutinize the sensitivity of the photocurrents to disorder next.
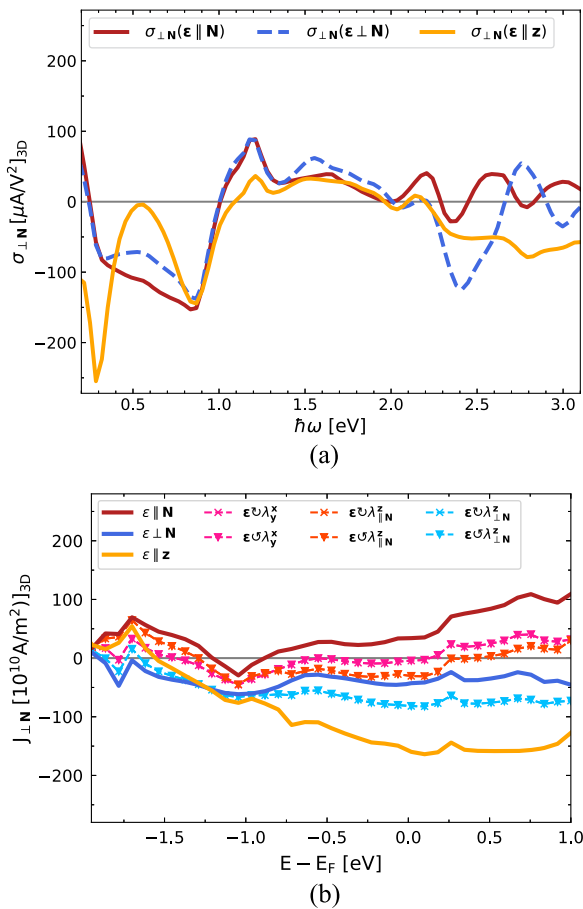
FIG. 5. Properties of in-plane photocurrents perpendicular to the Néel vector for $\hbar\omega = 3.00$ eV and a broadening of $\Gamma = 25$ meV. (a) Frequency dependence of the conductivity tensor projected onto the $[1\bar{1}0]$ direction for different cases of linearly polarized light. The Fermi level was set to the true Fermi level of Mn$_2$Au. (b) Photocurrent $J_{\perp \mathbf{N}}$ as a function of band filling in Mn$_2$Au. At the true Fermi level, the largest photocurrent arises in response to laser light linearly polarized along z. Note the difference in the band filling behavior compared to the case with another frequency and lifetime shown in Fig. 2.

3. Effect of quasiparticle lifetime

In this section, the dependence of the photocurrents on the quasiparticle lifetime when approaching the clean limit (i.e., broadening parameter $\Gamma \to 0$) is analyzed. We consider positive and negative Γ values to identify the magnetic origin of photocurrents. By analyzing the Γ-scaling of the photocurrents, it is also possible to identify the role of different quantum geometric quantities.[22,47–49] A general understanding of current photoresponse suggests that three terms can be identified that differ in their scaling behavior with respect to Γ: a Drude term quadratic in the lifetime broadening, a term probing the Berry curvature dipole, which is linear in the lifetime broadening, and a term probing the quantum metric dipole independent of the lifetime broadening.[22] However, the Berry curvature itself and, therefore, the Berry curvature dipole term are expected to vanish in $\mathcal{PT}$-symmetric

systems,[22] leaving only the Drude and the quantum metric dipole terms.

We show in Figs. 6(a)–6(c) the results of our calculations for $J_{\perp \mathbf{N}}$, $J_{\parallel \mathbf{N}}$, and J_z currents arising in response to different types of pulses of frequency $\hbar\omega = 3.0$ eV in a moderate range of positive and negative Γ values up to 200 meV. We observe that at 25 meV broadening, $J_{\perp \mathbf{N}}$ is as large as -150×10^{10} A/m^2 in the case of linearly z-polarized light [orange line in (a)], and a comparable current magnitude for the other two cases of in-plane polarizations [red and blue lines in (a)] is visible. Sizable responses to circularly polarized light—which are helicity independent averages of the response for two linear polarizations defining the plane of rotation—are also visible in $J_{\perp \mathbf{N}}$. These contributions can thus be associated with the LPGE. On the other hand, the other two components of the photocurrent—$J_{\parallel \mathbf{N}}$ and J_z—are an order of magnitude smaller over the entire range of Γ, but they are helicity-switchable. These photocurrents can thus be associated with the CPGE. While the LPGE currents are sizable for all three shown directions of linear polarization, the CPGE responses are only present for a specific plane of rotation of light for a given direction of the resulting current and given Néel vector orientation.

Notably, computed LPGE and CPGE responses are qualitatively different with respect to a reversal in the sign of Γ. This is indeed expected, as it is known that the LPGE and CPGE currents exhibit different behavior under time reversal operation $\mathcal{T}$; it can be shown that the LPGE is even under $\mathcal{T}$ for magnetization-independent and $\mathcal{T}$-odd for magnetization-dependent components of the conductivity tensor. However, in $\mathcal{PT}$-symmetric materials, the $\mathcal{P}$-symmetry is broken only by the magnetization and not by the crystal structure itself, and the magnetization-independent part of LPGE is expected to vanish. Indeed, such a magnetization dependent linear photogalvanic effect was predicted in the 2D antiferromagnetic $\mathcal{PT}$-symmetric insulator CrI$_3$ and proposed for 3D $\mathcal{PT}$-symmetric AFMs such as Mn$_2$Au.[46]

The behavior of the computed currents under Γ-reversal can now be understood by realizing that switching the sign of the quasiparticle lifetime is equivalent to a reversal of the Néel vector. Indeed, the linear photocurrent $J_{\perp \mathbf{N}}$ is odd with respect to the broadening, while the circular responses $J_{\parallel \mathbf{N}}$ and J_z are even in Γ. In conclusion, the LPGE photocurrents can be switched by a reversal of the Mn magnetic moments and, at certain laser frequencies, also by changing the orientation of the linearly polarized light. The CPGE photocurrents can only be switched by changing the light helicity and are one order of magnitude smaller as compared to the LPGE photocurrents.[50]

IV. INVERSE FARADAY EFFECT

In this section, we discuss the properties of the light-induced spin polarization, also known as the *inverse Faraday effect* (IFE), which is believed to play a crucial role in optical switching and the optical dynamics of antiferromagnets[6,7,9,28,30] in Mn$_2$Au. We compute and analyze the overall induced spin moment in the unit cell, δS^+, defined as the sum of all induced spin moments in the unit cell, as well as the *staggered* component of the induced spin, defined as the difference between the moments on different Mn sublattices: $\delta S^- = \frac{1}{2}[\delta S(\text{Mn}_A) - \delta S(\text{Mn}_B)]$. The results of our calculations of δS^+ and δS^- as a function of Γ (at $\hbar\omega = 3.0$ eV) and frequency (at
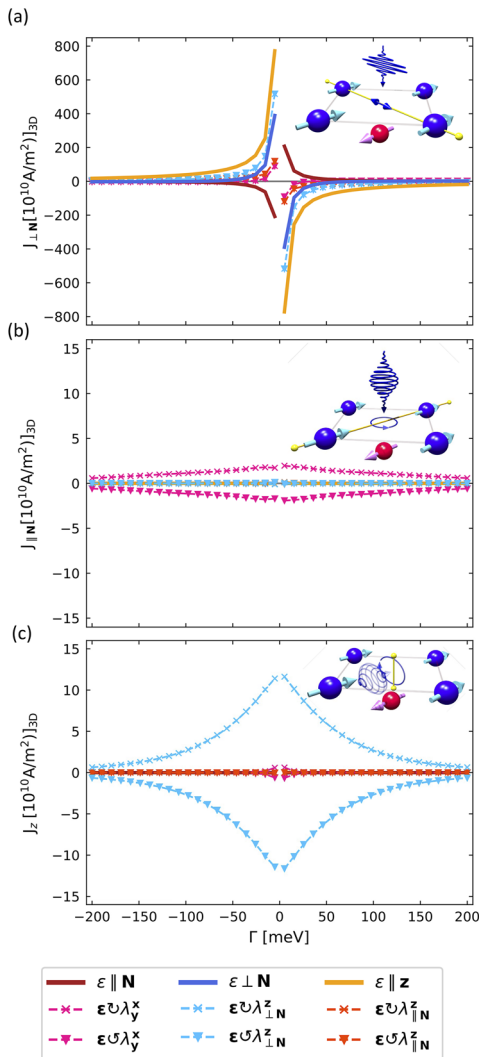
FIG. 6. Dependence of the photocurrents on the broadening parameter Γ at the true Fermi energy of Mn$_2$Au. The dependence of (a) $J_{\perp\mathbf{N}}$, (b) $J_{\parallel\mathbf{N}}$, and (c) J_z is shown for $\hbar\omega = 3.00$ eV for different types of laser pulses. For more details, see the text.

FIG. 7. Inverse Faraday effect in Mn$_2$Au. (a) and (b): Shown is the Γ dependence of total (a) and staggered (b) spin density, δS^+ and δS^-, respectively, for a laser frequency of $\hbar\omega = 3.00$ eV. In (c) and (d), the frequency dependence of the total (c) and staggered (d) laser induced spin, perpendicular and parallel to the Néel vector, respectively, is shown for $\Gamma = 25$ eV. In (e)–(g), the dependence of (e) parallel, $\delta S^+_{\parallel\mathbf{N}}$, (f) perpendicular, $\delta S^+_{\perp\mathbf{N}}$, and (g) z-component, δS^+_z, of the total spin density on the orientation of the polarization vector of linearly polarized light is shown. In each case, the polarization is rotated in the same plane in which the circularly polarized light rotates in (a).

$\Gamma = 25$ meV) are presented in Fig. 7. Similarly to previously discussed photocurrents, the induced spin is projected onto the z-, $\parallel\mathbf{N}$-, and $\perp\mathbf{N}$-directions.

We observe that the integrated induced spin, Fig. 7(a), is most sizable for the two in plane components, $\delta S^+_{\parallel\mathbf{N}}$ and $\delta S^+_{\perp\mathbf{N}}$, which exhibit a magnitude of the order of $1 \times 10^{-6}\hbar/2$ at 25 meV broadening at the frequency of $\hbar\omega = 3.00$ eV. All components are finite only when the direction of the induced spin density is along the normal of the plane of rotation of circularly polarized light, and they can be switched by the sense of light helicity, as expected from the IFE.[28] Each component, however, shows a unique frequency dependence: as Fig. 7(c) shows, the frequency dependence of the perpendicular in-plane spin density $\delta S^+_{\perp\mathbf{N}}$ can reach up to $5 \times 10^{-6}\hbar/2$ at the
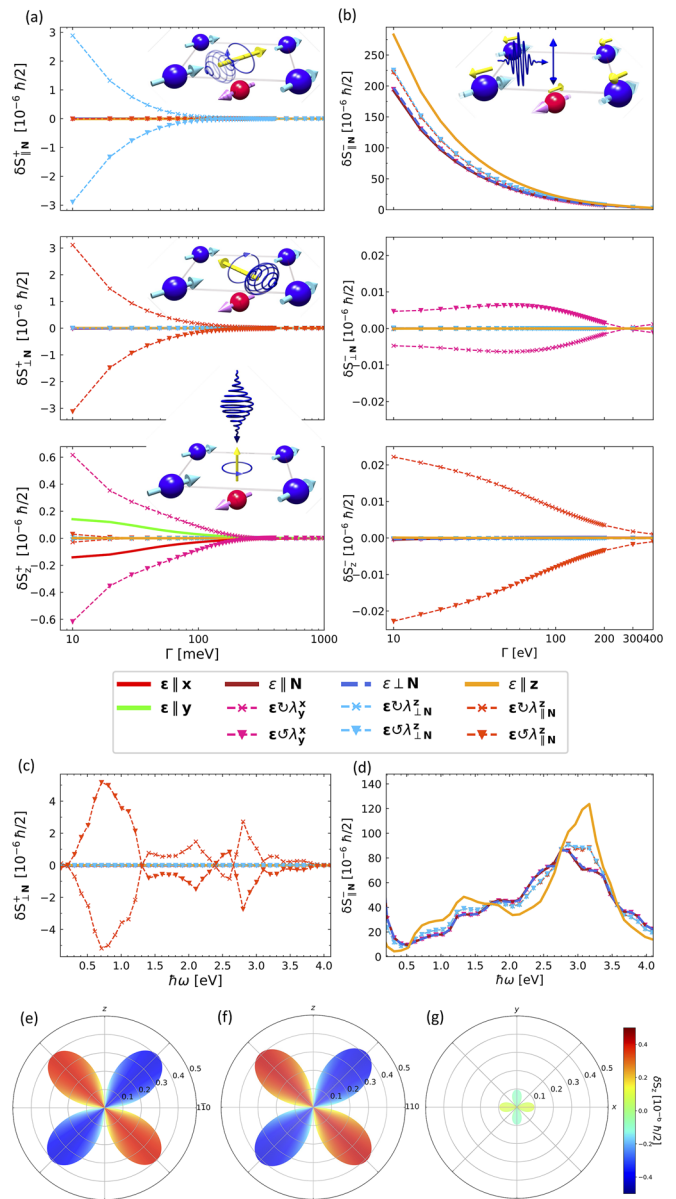
frequency of 800 meV. The in-plane component, which is parallel to the Néel vector (not shown), on the other hand, does not exceed a value of $\sim1.5 \times 10^{-6}\hbar/2$ throughout the entire frequency range.

The out-of-plane component of the induced spin δS_z^+ is significantly smaller than the other two components: at 25 meV of broadening, $\delta S_z^+ \approx 0.35 \times 10^{-6} \, \hbar/2$, which is more than two times smaller than the in-plane components. However, it shows the slowest decay toward larger broadening values, and it is comparable in magnitude to the in-plane components for Γ above 100 meV. In the range of Γ from 20 meV up to almost 200 meV, the z-component shows an almost perfect linear decrease when plotted vs Γ on a logarithmic scale, indicating a $\sim \log(\Gamma)$ behavior, whereas the in-plane components show a much quicker decay in this region.

Recently, we predicted that a laser-induced torque in Mn_2Au can be generated not only by circular but also by linearly polarized light.[42] Our calculations of the IFE are in complete agreement with the results of the latter work in terms of the symmetry of linear δS^+ and δS^-. For example, we can see in Fig. 7(a) that a non-vanishing δS_z^+ can arise in response to light polarized linearly along the x- and y-directions but not when the light polarization is along the $\perp\mathbf{N}$ and $\|\mathbf{N}$ directions. The overall dependence of δS_z^+, with $\hbar\omega = 3.00$ eV and $\Gamma = 25$ meV, on the orientation of linearly polarized light within the xy-plane is shown in Fig. 7(g). In analogy to δS_z^+, the components $\delta S_{\|\mathbf{N}}^+$ and $\delta S_{\perp\mathbf{N}}^+$ can also be driven by linearly polarized light if the light polarization is confined to the plane whose normal is aligned with the induced spin density (the same plane in which a finite response to circularly polarized light occurs). Figures 7(e) and 7(f) display the dependence of $\delta S_{\|\mathbf{N}}^+$ and $\delta S_{\perp\mathbf{N}}^+$ on the orientation of linearly polarized light in the corresponding planes. Our findings are in full agreement with the symmetry analysis provided in Table I of Ref. 42: the overall induced spin responses in xy-plane $\delta S_{\|\mathbf{N},\perp\mathbf{N}}^+$ correspond to symmetry tensors Nos. 3 and 29, while the out-of-plane component δS_z^+ corresponds to the average of tensors Nos. 24 and 30, which describe the scenario of the Néel vector along the x- and y-directions, respectively. The findings of laser induced magnetization presented in this work are, therefore, intimately linked to the laser induced torques found in Ref. 42. For example, the induced magnetization δS_z^+ shown in the third raw of Fig. 7(a) drives the torque T_z presented in Fig. 1 of Ref. 42.

While the magnitude of the in-plane responses is overall significantly larger than that of δS_z^+, the dependence of the sign of the spin polarization on the light polarization and a non-trivial angular dependence of the signal suggest that a very complex spin response in Mn_2Au can be driven by the "off-axis" linearly polarized pulses. While the uniform response δS^+ is effectively equivalent to an effect of canting or the formation of weak ferromagnetism, the staggered component of IFE, δS^-, can give rise to a Néel-type torque on the staggered magnetization[51,52] or result in a staggered modulation of the local moments. As for the latter, while the Néel type torques are being currently intensively explored with respect to electrical and optical switching of antiferromagnetic order,[5,12,18,52,53] recently, a large staggered IFE was reported in AFM CrPt,[9] where a direct quenching of the magnetic moments on the Cr sublattices was achieved by circularly polarized light. The reported quenching was identified as the origin of ultrafast optical switching of the Néel vector in CrPt,[9] highlighting the importance of staggered IFE in AFM materials. Notably, the properties of δS^- that we compute and present in Fig. 7(b) are quite different from the properties of δS^+ in many respects.

First, the staggered IFE components perpendicular to the Néel vector, $\delta S_{\perp\mathbf{N}}^-$ and δS_z^-, are one to two orders of magnitude smaller than the corresponding components of δS^+, and they exhibit a qualitatively different behavior with the disorder. Second, the staggered response parallel to the Néel vector, $\delta S_{\|\mathbf{N}}^-$, is two orders of magnitude larger than δS^+, reaching as much as $10^{-4}\hbar/2$ at room temperature ($\Gamma = 25$ meV) in value. Moreover, the staggered response is finite not only for circularly polarized light but also for linearly polarized light, with circular responses being helicity-independent. Therefore, among all the discussed components of δS^- and δS^+, $\delta S_{\|\mathbf{N}}^-$ behaves like an LPGE effect, while all the other components exhibit a CPGE-like behavior. Remarkably, the frequency dependence of $\delta S_{\|\mathbf{N}}^-$ is also very distinct: as we see in Fig. 7(d), in the entire frequency range, the staggered response has the same amplitude for light linearly or circularly polarized within the xy-plane. For the latter, the largest response of $85 \times 10^{-6}\hbar/2$ occurs at $\hbar\omega = 2.8$ eV. For linear polarization along z, an even larger peak of $125 \times 10^{-6}\hbar/2$ is visible at $\hbar\omega = 3.1$ eV. Note that the sign of $\delta S_{\|\mathbf{N}}^-$ is preserved for the entire frequency band, which is in stark contrast to other components. Overall, the complexity of laser-induced flavors of spin polarization in Mn_2Au suggests that the physics of laser-induced spin currents in this material, which we consider next, can also be very rich.

V. LASER INDUCED SPIN CURRENTS

In solids, the interaction of light with matter mediated by spin–orbit interaction suggests the exciting possibility of generating pure spin currents with light. Historically, nonmagnetic semiconductors were first found to host a spin Hall effect,[54] which was suggested to generate spin currents under radiation with circularly polarized light.[55] Later on, an all-optical generation of spin currents via a transfer of optical angular momentum into a spin-orbit-coupled semiconductor was reported.[56] Recently, an optical generation of colossal spin currents, which are second order in the field, has been predicted theoretically for ferromagnets.[31] Moreover, $\mathscr{PT}$-symmetric collinear AFMs, such as those discussed here in Mn_2Au, were proposed as efficient sources of spin currents,[57] and a large spin circular photogalvanic effect was predicted for $\mathscr{PT}$-symmetric antiferromagnetic insulators.[58] Ultrafast generation of pure spin currents via the spin photogalvanic effect was predicted in collinear insulating 2D AFMs.[59] It was also shown that in noncentrosymmetric systems that still hold mirror symmetry, pure bulk spin currents can be generated even by means of linearly polarized light.[60]

A. Symmetry analysis

In this section, we investigate laser-induced spin-polarized photocurrents, or *spin photocurrents*, Q_i^j, propagating along direction i with spin polarization along direction j, arising in response to linearly and circularly polarized light in Mn_2Au. Photospincurrents that are independent of the Néel vector are described by axial tensors of the fourth rank. We find that axial tensors of the fourth rank are not allowed by symmetry in Mn_2Au. Spin photocurrents that are linear in the Néel vector are described by staggered polar tensors of the fifth rank,

$$Q_i^j = \chi_{ijklm}^{(5sp)} E_k E_l^* N_m. \tag{11}$$

We find that there are 31 staggered polar tensors of rank 5 allowed by symmetry in Mn_2Au. We list them in Table II.

TABLE II. List of staggered polar tensors of rank 5 allowed by symmetry in Mn_2Au. The notation introduced in Eq. (8) is used.

No.	$\chi_{ijklm}^{(5sp)}$	No.	$\chi_{ijklm}^{(5sp)}$
1	$\langle 22\,113 \rangle + \langle 11\,223 \rangle$	17	$\langle 31\,331 \rangle + \langle 32\,332 \rangle$
2	$\langle 21\,213 \rangle + \langle 12\,123 \rangle$	18	$\langle 13\,331 \rangle + \langle 23\,332 \rangle$
3	$\langle 33\,333 \rangle$	19	$\langle 13\,313 \rangle + \langle 23\,323 \rangle$
4	$\langle 12\,213 \rangle + \langle 21\,123 \rangle$	20	$\langle 13\,133 \rangle + \langle 23\,233 \rangle$
5	$\langle 31\,111 \rangle + \langle 32\,222 \rangle$	21	$\langle 11\,333 \rangle + \langle 22\,333 \rangle$
6	$\langle 31\,221 \rangle + \langle 32\,112 \rangle$	22	$\langle 12\,321 \rangle + \langle 21\,312 \rangle$
7	$\langle 33\,311 \rangle + \langle 33\,322 \rangle$	23	$\langle 11\,131 \rangle + \langle 22\,232 \rangle$
8	$\langle 13\,221 \rangle + \langle 23\,112 \rangle$	24	$\langle 11\,113 \rangle + \langle 22\,223 \rangle$
9	$\langle 32\,121 \rangle + \langle 31\,212 \rangle$	25	$\langle 21\,321 \rangle + \langle 12\,312 \rangle$
10	$\langle 23\,121 \rangle + \langle 13\,212 \rangle$	26	$\langle 22\,311 \rangle + \langle 11\,322 \rangle$
11	$\langle 32\,211 \rangle + \langle 31\,122 \rangle$	27	$\langle 21\,231 \rangle + \langle 12\,132 \rangle$
12	$\langle 23\,211 \rangle + \langle 13\,122 \rangle$	28	$\langle 22\,131 \rangle + \langle 11\,232 \rangle$
13	$\langle 13\,111 \rangle + \langle 23\,222 \rangle$	29	$\langle 31\,313 \rangle + \langle 32\,323 \rangle$
14	$\langle 11\,311 \rangle + \langle 22\,322 \rangle$	30	$\langle 31\,133 \rangle + \langle 32\,233 \rangle$
15	$\langle 12\,231 \rangle + \langle 21\,132 \rangle$	31	$\langle 33\,113 \rangle + \langle 33\,223 \rangle$
16	$\langle 33\,131 \rangle + \langle 33\,232 \rangle$		

B. Properties of spin photocurrents

We compute the magnitude of a spin current Q_A^B, propagating along direction **A** with spin polarization along direction **B** as a function of Γ at $\hbar\omega = 3.0$ eV, presenting the results in Figs. 8 and 9. First, we discuss the spin currents propagating in the xy-plane, shown in Fig. 8. In the latter case, the most sizable spin photocurrents are $Q_{\parallel N}^{\parallel N}$ and $Q_{\perp N}^{\parallel N}$ (Fig. 8, upper panel), achieved by circularly polarized light with the in-plane direction of the polarization plane normal, with amplitudes reaching as much as $\sim 150 \times 10^{10}\ \hbar/(2e)$ A/m^2 at room temperature ($\Gamma = 25$ meV). Both components can be switched in sign by light helicity. The components with the spin polarization perpendicular to the Néel vector, $Q_{\parallel N}^{\perp N}$ and $Q_{\perp N}^{\perp N}$ (Fig. 8, middle panel), are somewhat smaller in magnitude but still significant. From the plots, an apparent symmetry is visible: at a given direction of spin polarization, along or perpendicular to **N**, the direction of the current in-plane can be rotated by changing the in-plane direction of the polarization plane normal. The spin photocurrents propagating in the xy-plane correspond to symmetry tensors Nos. 14, 15, 22, 23, and 25–28 of Table II.

The spin current flowing parallel to the Néel vector with spins pointing along the z-direction, $Q_{\parallel N}^z$, shown in the lower panel of Fig. 8, is the only in-plane component responding to linearly polarized light, with amplitudes reaching $75 \times 10^{10}\ \hbar/(2e)$ A/m^2 at $\Gamma = 25$ meV. Here, the corresponding circular spin currents are also sizable but are helicity-independent and are given by the averages of the linear polarized responses; this marks $Q_{\parallel N}^z$ as a manifestation of LPGE. The LPGE-like spin photocurrent in response to light linearly polarized within the xy-plane is supported by symmetry tensor No. 13 of Table II, while the response to light linearly polarized along z corresponds to tensor No. 18.

In analogy to the case of charge photocurrents shown in Fig. 6, LPGE-like $Q_{\parallel N}^z$ decays much slower with Γ than the rest of the spin currents, which are CPGE-like. Again, in analogy to charge photocurrents, the spin polarized current $Q_{\parallel N}^z$ changes sign when

rotating the in-plane linear polarization by 90° in the xy-plane (red and blue solid lines) or into the z-axis (orange solid line). A given linearly polarized pulse thus not only induces a charge current flowing perpendicular to **N**, $J_{\perp N}$, but also a spin-polarized current $Q_{\parallel N}^z$, which is perpendicular to $J_{\perp N}$. This can be interpreted as an *optical analogon of the spin Hall effect*, as discussed in Subsection V C (see also Fig. 10).

Finally, in Fig. 9, we display the spin photocurrents flowing out of the plane along the z-direction for different orientations of the spin polarization. Two types of spin currents can be distinguished here: the LPGE-like spin current $Q_z^{\parallel N}$, shown in Fig. 9(a), and CPGE-like helicity-dependent spin currents, with spin polarization perpendicular to **N** (pink curve) and along z (orange curve), shown in Fig. 9(b). The LPGE-currents in Fig. 9(a) in response to light linearly polarized in the xy-plane correspond to averages of symmetry tensors Nos. 5 and 6 of Table II, while the response to light polarized along z is governed by symmetry tensor No. 17. The CPGE-like spin photocurrent Q_z^z in Fig. 9(b) corresponds to an average of symmetry tensors Nos. 7 and 16 of Table II, and the $Q_z^{\perp N}$ current to tensors Nos. 9 and 11. Among the two flavors of spin currents, in accordance with our previous observations, LPGE-currents are subdominant and exhibit a non-trivial dependence on broadening: the majority of circular currents, being an average over linear currents of opposite sign and non-trivial Γ-dependence, change their sign at the value of broadening of about 30 meV. By generalizing our observations, we can conclude that spin currents with spins aligned with the direction of propagation, i.e., Q_a^a with $a \in \{\parallel N, \perp N, z\}$, only respond to circularly polarized light rotating in the plane spanned by the Néel-vector and the z-axis. On the other hand, spin currents of the type Q_a^b, for $a \neq b \in \{\parallel N, \perp N, z\}$, are always driven by the same type of pulse as Q_b^a spin currents.

Owing to the fact that only a single component, slowly decaying with respect to the broadening parameter Γ, flows within the xy-plane and along z, we envisage the spin photocurrents arising in response to linearly polarized light as optimally suited for experimental realization. Since the sizable spin photocurrents are induced for all orientations of the linearly polarized light, remarkable flexibility in terms of possible geometric setups is present in this scenario. The spin photocurrent flowing along the Néel vector with spin polarization along z is larger by an order of magnitude as compared to the out-of-plane LPGE-like spin photocurrent, and thus the former in-plane component seems best suited to be utilized in spintronics devices. Although experimentally challenging,[61,17] in-plane spin currents can be injected and used to exert a torque on the magnetization of a ferromagnet interfaced with Mn_2Au,[61] a situation where various device concepts consisting of a heavy metal as a spin current generator and a ferromagnet have been suggested in the past.[62–66] Our findings elevate these effects to the optical realm, as will be further stressed in Sec. V C. Moreover, we speculate that the injection of the spin photocurrent into a heavy substrate can be used to drive an inverse spin Hall effect and corresponding THz radiation, which can be utilized for the detection of the Néel order and Néel vector orientation.[67,68]

We recall that LPGE charge photocurrents, presented in Fig. 6, were found to be odd under sign reversal of the broadening, while CPGE charge photocurrents showed an even behavior, identifying both as purely magnetic photocurrents. In the Keldysh formalism, the difference between the charge and spin photocurrent comes
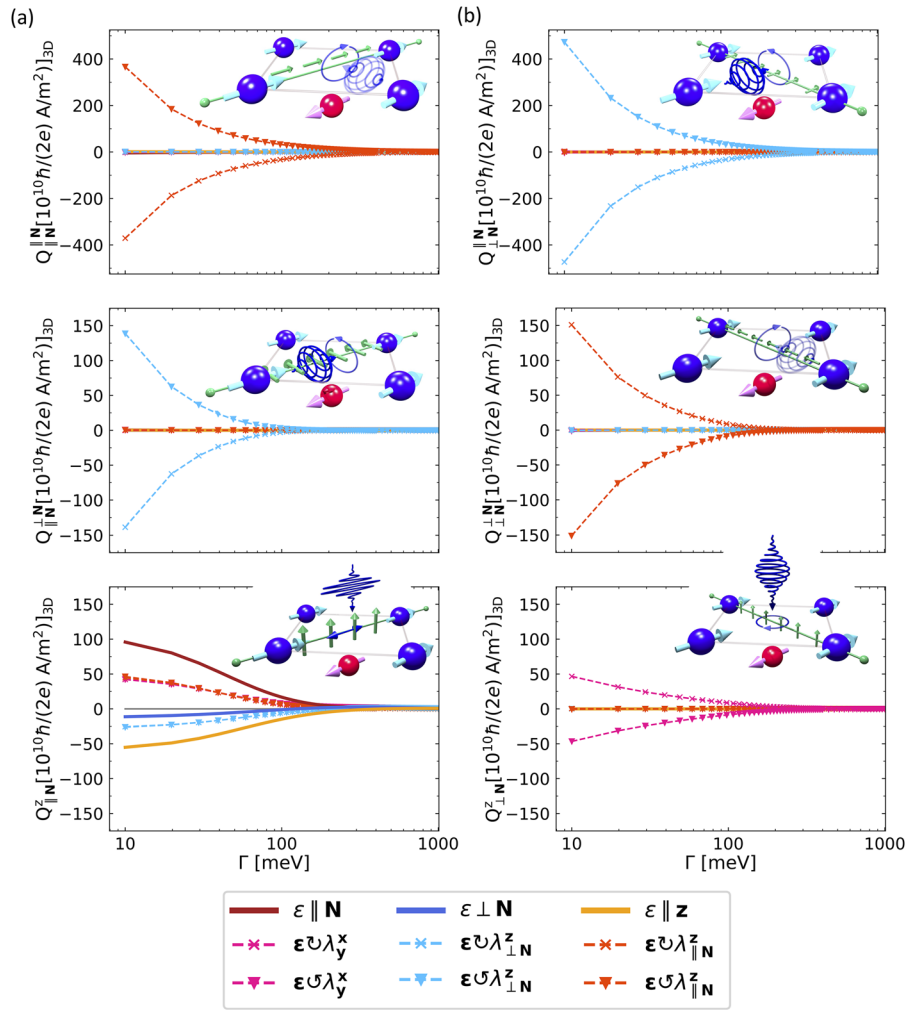
FIG. 8. Laser-induced spin currents as a function of broadening Γ for a frequency of $\hbar\omega = 3.00$ eV. Left column (a) shows the spin currents flowing parallel to the Néel vector, and the right column (b) perpendicular to the Néel vector for different directions of spin polarization as indicated by yellow arrows. In our nomenclature, $Q_{\mathbf{A}}^{\mathbf{B}}$ denotes a spin current propagating along direction $\mathbf{A}$ with spin polarization along direction $\mathbf{B}$.

from replacing one of the velocity operators v_i with the spin-velocity operator $\{v_i, \tau_s\}$, where τ_s is one of the Pauli matrices. Since τ_s is odd under $\mathscr{T}$, the behavior of spin photocurrents with respect to the reversal in Γ is opposite to that of charge photocurrents. Magnetic LPGE-like spin photocurrents are, therefore, expected to be even under sign reversal of Γ, and magnetic CPGE-like spin photocurrents are odd. We checked the behavior of the spin currents presented in Figs. 8 and 9, with respect to a sign reversal of the broadening and found all, LPGE- and CPGE-like responses to be purely magnetic.

C. Photospin Hall effect in Mn₂Au

At this point, let us summarize our findings for a simple case of light linearly polarized along $\mathbf{N}$, $\mathbf{N}\|[110]$. In this case, the only type of photoinduced charge current is $J_{\perp\mathbf{N}}$, the only non-vanishing

photo-induced spin polarization is $\delta S_{\|\mathbf{N}}^-$, and there are two types of pure spin current: $Q_z^{\|\mathbf{N}}$ and $Q_{\|\mathbf{N}}^z$. Both of these spin currents nominally satisfy the spin Hall effect geometry, i.e., the direction of spin current propagation and its spin polarization are orthogonal to each other and to the direction of $J_{\perp\mathbf{N}}$. Of these two, we will consider below only $Q_{\|\mathbf{N}}^z$ since it is larger in magnitude than the former (which is nominally a manifestation of the anisotropic spin Hall effect in SHE language[69]), while their properties, discussed below, are similar. It, therefore, seems insightful to scrutinize a possible relation between the three LPGE-like types of quantities $J_{\perp\mathbf{N}}$, $Q_{\|\mathbf{N}}^z$, and $\delta S_{\|\mathbf{N}}^-$.

We first compare the behavior of $J_{\perp\mathbf{N}}$ and $Q_{\|\mathbf{N}}^z$ by plotting in Figs. 11(a) and 11(b) their frequency dependence for three flavors of the linearly polarized light. What we realize immediately is that the considered charge and spin currents exhibit some qualitative
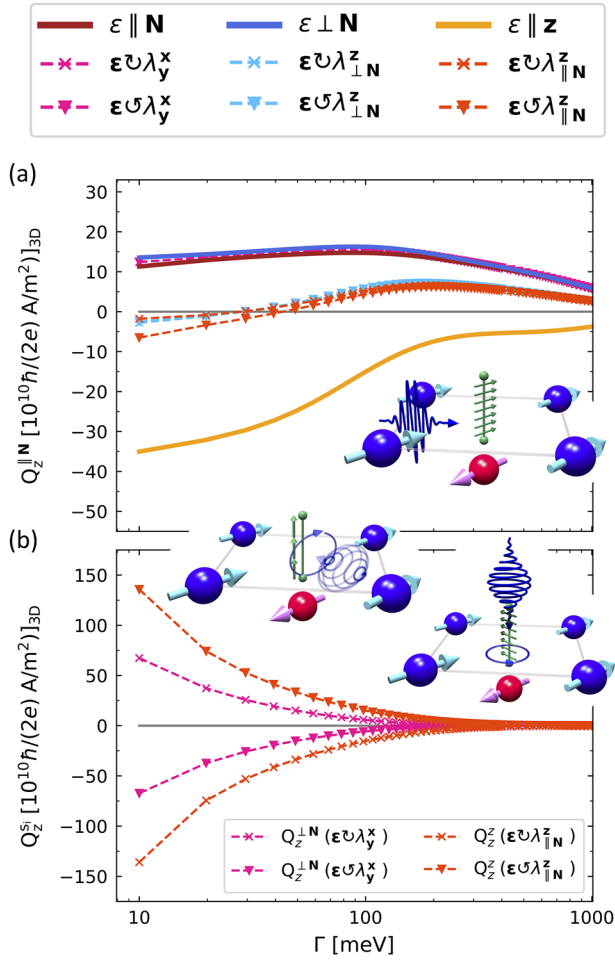
FIG. 9. Laser-induced spin currents as a function of broadening Γ for a frequency of $\hbar\omega = 3.00$ eV. (a) Spin currents flowing along z with spin polarization along the Néel vector. (b) Spin currents flowing along z for spin polarization along z and perpendicular to the Néel vector.
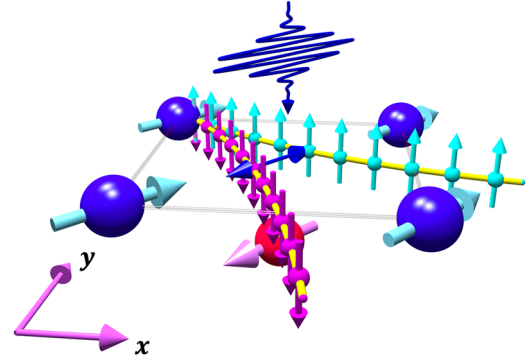

FIG. 10. Sketch of the photospin Hall effect in Mn$_2$Au. In Mn$_2$Au, a linearly polarized light (shown with a wavy arrow; the polarization direction shown with a blue two-sided arrow in the center of the plot) generates an in-plane charge photocurrent perpendicular to Néel vector **N** (given by the direction of the arrow on the "blue" sublattice of Mn atoms). Via the photospin Hall effect, the charge current generates a transverse spin current with spin polarization out of the plane, propagating along **N**. The effect of the spin-Hall-like spin-dependent deflection of electrons (small balls), whose spin is depicted with vertical blue and cyan little arrows, is shown by an effective curving of the electron trajectories.

as the normalized ratio between the charge and spin photocurrents, transverse to each other,

$$\Theta_{\text{PSH}} = \arctan \frac{Q^z_{\|\mathbf{N}}}{J_{\perp\mathbf{N}}}. \tag{12}$$

The practical meaning of the photospin Hall angle lies in providing the ability to predict the value of the generated transverse spin photocurrent given an experimentally measured value of the charge photocurrent. Figures 11(c) and 11(d) display the computed PSHA in Mn$_2$Au for various flavors of linearly polarized light plotted as a function of band filling (for $\hbar\omega = 3.0$ eV) and laser frequency (at the true Fermi energy), computed at $\Gamma = 25$ meV. Generally, we observe that around the true Fermi energy of Mn$_2$Au, the PSHA is relatively constant, acquiring the largest value for light polarized along **N**. From the frequency dependence of the PSHA, we learn about the rapidly oscillatory behavior of this quantity, suggesting that the ratio between the charge and spin currents can be tuned by the frequency not only in magnitude but also in sign.

To get a better feel for the microscopic origin of the photospin Hall effect, we look at the reciprocal space distribution of considered charge and spin currents at $\hbar\omega = 3.00$ eV in Figs. 11(e) and 11(f). The charge photocurrent $J_{\perp\mathbf{N}}$, shown in Fig. 11(e), exhibits competing regions of positive and negative sign in reciprocal space, which yield a net effect when integrated over the entire BZ. Shown in Fig. 11(f) is the distribution of $Q^z_{\|\mathbf{N}}$. Clearly, when compared to the charge photocurrent, the spin photocurrent displays a qualitatively different behavior in the BZ. Instead of competing regions of the positive and negative signs, the spin photocurrent is mostly driven by two symmetry-related hotspots in $+k_z$- and $-k_z$-layers, which both contribute with the same sign but are an order of magnitude smaller as compared to the hotspots of charge photocurrent, which are also positioned closer to the BZ boundary.

similarities with respect to ω. Both charge and spin photocurrents are enhanced in the region of smaller frequencies, where the responses are comparable in amplitude for two in-plane polarizations (red and blue curves), changing their sign at a frequency of $\hbar\omega = 1.00$ eV. In the frequency band of $\hbar\omega$ from 2 to 3.5 eV, a strong oscillatory behavior is visible for light linearly polarized in the xy-plane. At $\hbar\omega = 2.8$ eV, the spin photocurrent is maximized with a strong peak for light linearly polarized along **N** (red curve) and a negative peak for light polarized along z (golden curve). A corresponding peak for z-polarization is also visible at this frequency for the charge current.

Given the proper symmetry of the effect, as discussed earlier, it seems rewarding to interpret the relation between $J_{\perp\mathbf{N}}$ and $Q^z_{\|\mathbf{N}}$ in terms of a flavor of the spin Hall effect (see Fig. 10). We suggest referring to this effect as the *photospin Hall effect*, which can be characterized in terms of a *photospin Hall angle* Θ_{PSH}, PSHA, defined
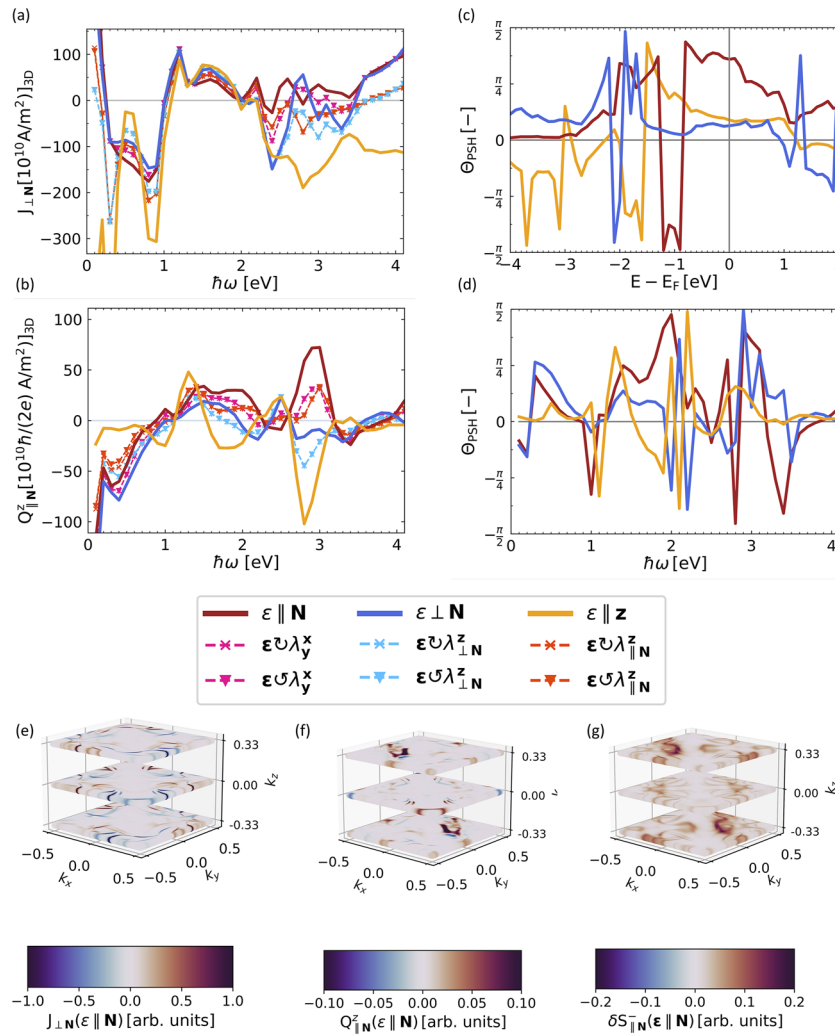
FIG. 11. Photospin Hall effect in Mn_2Au. (a) and (b) The frequency dependence of charge current $J_{\perp N}$ (a) and spin current $Q^z_{\parallel N}$ (b) for various types of incoming light pulse. In (a), the computed circular currents are averages of corresponding linear currents. In (c) and (d), the photospin Hall angle Θ_{PSH}, as defined in the text, is plotted vs the band filling at $\hbar\omega = 3.0$ eV (c) and frequency (d). (e)–(g) Brillouin zone distribution of $J_{\perp N}$ (e), $Q^z_{\parallel N}$ (f), and $\delta S^-_{\parallel N}$ (g), at the frequency of $\hbar\omega = 3.00$ eV. For all calculations, the broadening Γ was fixed to 25 meV.

Let us now take a look at laser-induced spin polarization $\delta S^-_{\parallel N}$. First of all, we find that the BZ distribution of this quantity, presented in Fig. 11(g), is qualitatively very similar to that of the spin current, especially with respect to the position and relative sign of major contributing hotspots, which might be related to the spin nature of both effects. Second, we also find some similarities between $\delta S^-_{\parallel N}$ and $Q^z_{\parallel N}$ in their dependence on laser frequency: the spin photocurrent, Fig. 11(f), exhibits local extrema at the frequency around $\hbar\omega = 2.8$ eV, which is also the case for photo-induced spin density, presented in Fig. 7(d). In addition, for linearly polarized along z light, all three quantities—the charge and spin photocurrents as well as nonequilibrium spin density—display a peak at $\hbar\omega = 1.2$ eV, which can be attributed to a large number of states available around that energy [see Figs. 1(c) and 1(d)]. Overall, we

thus find some level of correlation between the three quantities, which is also expected in the conventional d.c. physics of the linear in the field Rashba-Edelstein-like phenomena.[70,71]

VI. EFFECT OF CANTING

Antiferromagnets are naturally prone to the effect of canting away from collinear configuration, which can be characterized by the so-called vector chirality proportional to the vector product between the spins on two sublattices. Recently, we have shown that in bipartite canted antiferromagnets the behavior of the anomalous Hall effect (AHE) can be systematically categorized based on the crystal[72,73] and chiral flavors of the AHE , which are even and odd in vector chirality, respectively.[74] This separation has also been

generalized to the domain of magneto-optical phenomena and was shown to be crucial in understanding the temperature and magnetic field dependence of the AHE in antiferromagnets.[75] In AFMs, the chiral Hall effect directly probes the sense of chirality of the magnetic moments, as was also shown in the case of Mn_2Au.[74] Although the canting of magnetic moments is forbidden by the $\mathcal{PT}$-symmetry of the system, a symmetry lowering due to, for example, the application of an external magnetic field or deposition on a substrate can be used to induce canting. In this section, we introduce and study the chiral flavors of the photocurrents and the inverse Faraday effect in Mn_2Au.

A. Chiral photocurrents

Similarly to the case of the anomalous Hall effect,[74] we introduce the *crystal* and *chiral photocurrents* as symmetric $J^{(s)}$ and antisymmetric $J^{(a)}$ parts of the photocurrents upon switching the sign of chirality as given by the canting angle θ away from the $\|\mathbf{N}$-direction,

$$J^{(s/a)} = \frac{J(+\theta) \pm J(-\theta)}{2}, \tag{13}$$

where $J(\pm\theta)$ is the photocurrent evaluated in the system with spins canted by an angle $\pm\theta$ toward either the z- (out-of-plane canting) or the $\perp\mathbf{N}$-direction (in-plane canting) (see sketches in Fig. 12). As in the case of the anomalous Hall effect,[74] we expect the

symmetric, crystal photocurrents to closely follow the properties of collinear photocurrents studied earlier, at least for small canting angles, while marking the sensitive to the sense of chirality chiral photocurrents as a type of current that is characteristic of canted systems. Practically, we realize the effect of canting by applying an external exchange term to the Wannier interpolated Hamiltonian, as described in Ref. 74. Unless stated otherwise, we apply an exchange field B of 200 meV, keeping in mind that a field with a magnitude of ± 100 meV results in about $\pm 2°$ canting of Mn moments. We achieve the in-plane (IP) and out-of-plane (OOP) canting by applying the positive $(+\theta)$ and negative $(-\theta)$ exchange fields perpendicular to the Néel vector in-plane and along z, respectively.

We discuss in detail the case of out-of-plane canting, presenting in Fig. 12 the results for $J_{\perp\mathbf{N}}^{(s/a)}$ (left) and $J_{\|\mathbf{N}}^{(s/a)}$ (right) components as defined in Eq. (13) for a 200 meV exchange field applied along z. We observe that the symmetric perpendicular current, $J_{\perp\mathbf{N}}^{(s)}$, Fig. 12(a), arises in response to linearly polarized light and shows an almost identical frequency dependence as the corresponding photocurrent for the collinear spin configuration shown in Fig. 5. The symmetric parallel current, $J_{\|\mathbf{N}}^{(s)}$, Fig. 12(b), responds only to light circularly polarized in the xy-plane, which is also the case for the collinear scenario. We have checked that for all considered responses, the expectation that the symmetric responses would closely resemble the uncanted ones generally holds true very well, and we thus discuss in the following only the chiral contributions.

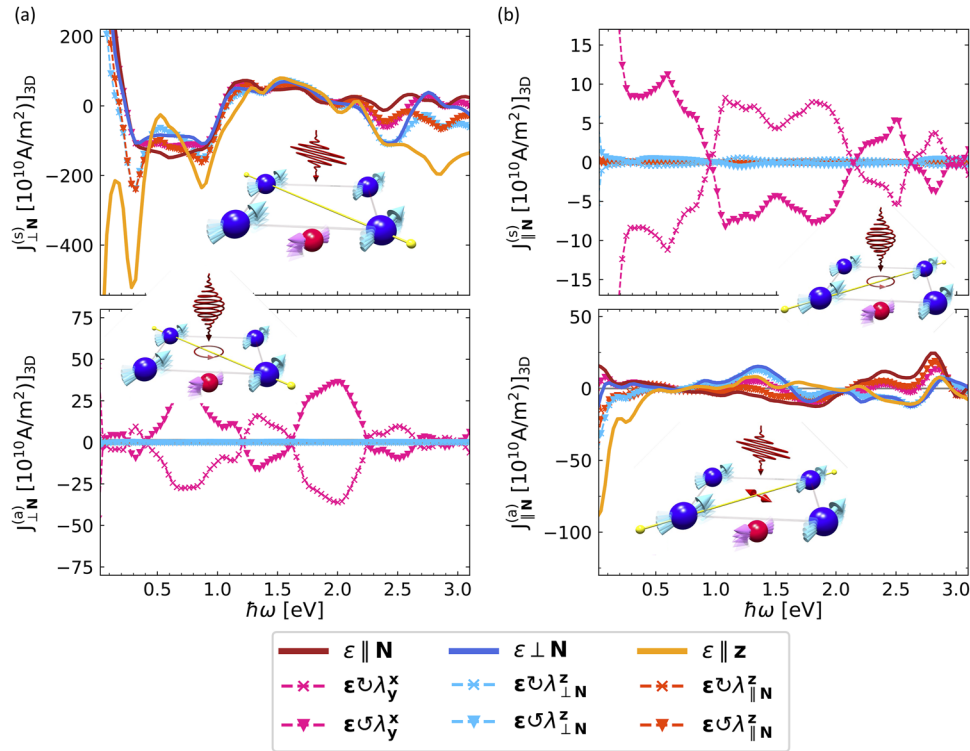**FIG. 12.** Symmetric (upper panel) and antisymmetric (lower panel) charge photocurrents at 200 meV canting along z, which are (a) perpendicular and (b) parallel to the Néel vector, as a function of the laser frequency for the broadening of 25 meV.

The chiral photocurrent $J_{\perp N}^{(a)}$ shown in Fig. 12(a) is driven by xy-circularly polarized light and is in contrast to the symmetric component, helicity-switchable, with the largest amplitude $J_{\perp N}^{(a)} \approx \pm 37 \times 10^{10}$ A/m^2 at the laser frequency of $\hbar\omega = 2.0$ eV. The chiral photocurrent flowing parallel to the Néel vector, Fig. 12(b), is comparable in amplitude with $J_{\parallel N}^{(a)} \approx 28 \times 10^{10}$ A/m^2 at $\hbar\omega = 2.8$ eV.

In contrast to the symmetric current for this component, $J_{\parallel N}^{(a)}$ is driven by linearly polarized light, and its circular part is given by an average over linear components. At finite frequencies, both chiral photocurrents are comparable in magnitude to their respective crystal counterparts. This is unexpected given a small degree of canting of the moments; however, this observation falls into the philosophy of a generally very prominent chiral response in AFMs, also observed for the anomalous Hall effect.[74]

We note that due to symmetry, chiral charge photocurrents respond to the same type of field as collinear spin photocurrents if the spin polarization of the spin photocurrents is along the direction of the applied canting field (for example, $J_{\parallel N}^{(a)}$ and $Q_{\parallel N}^z$

both show LPGE-like responses). Interestingly, chiral photocurrent response to linearly polarized light is only present if the exchange field is applied out of the plane. In the case of in-plane canting, sizable chiral photocurrents are also present, but only in response to circularly polarized light. The presence of chiral photocurrents in response to linearly polarized light might, therefore, be utilized as a proxy for an out-of-plane switching path accompanied by canting.

B. Chiral IFE and chiral spin photocurrents

Motivated in part by our observation of strong chiral photocurrents of charge and given a strong recent interest in the physics and properties of spin currents in chiral systems,[76–79] we finally discuss the modifications to IFE and spin photocurrents brought about by canting in Mn$_2$Au. Analogously to Eq. (13), we define the symmetric (crystal) and antisymmetric (chiral) components of the laser induced spin density and spin photocurrent with respect to a canting by angle θ as
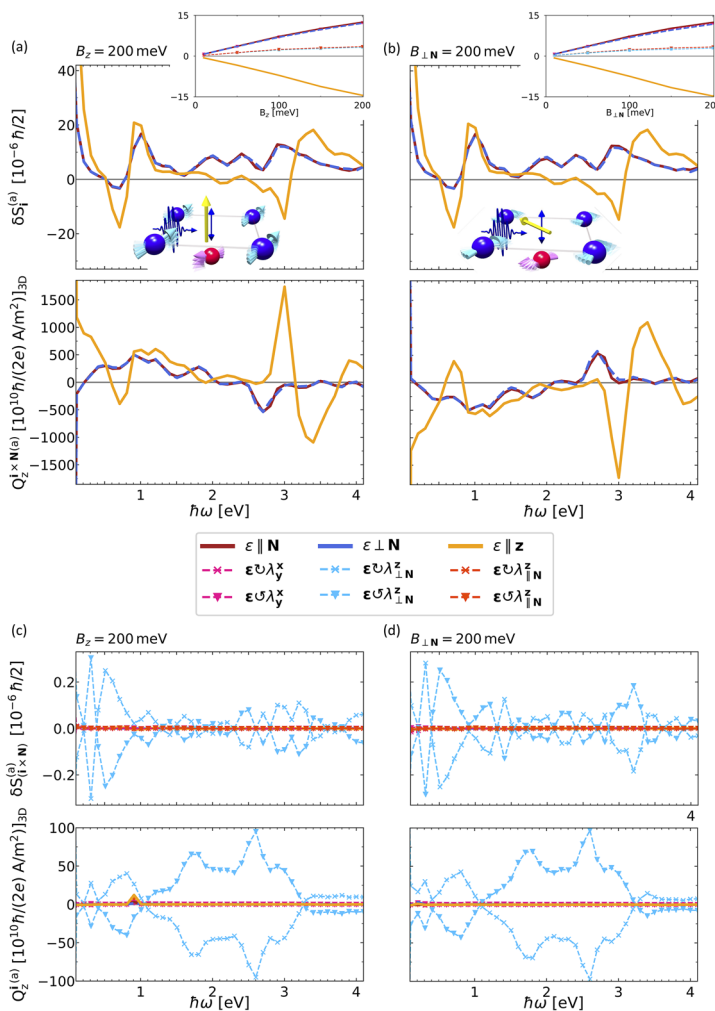

FIG. 13. Antisymmetric spin responses as a function of light frequency for (a) and (c) in-plane canting (IP, exchange field B along $\mathbf{i} \perp \mathbf{N}$) and (b) and (d) out-of-plane canting (OOP, exchange field B along $\mathbf{i} \parallel \mathbf{z}$). Shown are the laser-induced nonequilibrium spin density and the associated spin photocurrent. (a) and (b): The exchange field applied along $\mathbf{i}$ drives an LPGE-like chiral spin density parallel to the field. The associated LPGE chiral spin photocurrent flows along z, and it is polarized along $\mathbf{i} \times \mathbf{N}$. Note the colossal magnitude of the chiral spin currents. The insets show the dependence of the antisymmetric spin density on the strength of the applied exchange field for various laser polarizations (at $\hbar\omega = 3.0$ eV). (c) and (d) The exchange field also drives a CPGE-like chiral spin density along the $\mathbf{i} \times \mathbf{N}$ direction. The associated CPGE-like spin photocurrent propagates along z, and it is polarized perpendicular to the induced spin density along $(\mathbf{i} \times \mathbf{N}) \times \mathbf{N} = \mathbf{i}$. The broadening for all calculations has been taken at the value of 25 meV.

$$\delta S^{a/s} = \frac{\delta S^+(+\theta) \pm \delta S^+(-\theta)}{2},$$

$$Q^{a/s} = \frac{Q(+\theta) \pm Q(-\theta)}{2}. \tag{14}$$

Note that we consider only the chiral component of the total photo-induced spin density δS^+ and spin photocurrent Q, as we did not find either qualitative changes or significant magnitude in other components upon canting.

In Fig. 13, we present the frequency dependence of the LPGE-like (a) and (b) and CPGE-like (c) and (d) chiral nonequilibrium spin density and spin current for the IP (a) and (c) and OOP (b) and (d) canting. Displayed in Figs. 13(a) and 13(b) is the chiral spin density induced along the direction **i** of the applied IP and OOP exchange fields. The induced spin density is clearly LPGE-like with a sizable magnitude for all orientations of the linearly polarized light. Comparing the spin density responses in (a) and (b), we realize that induced δS_i^a does not at all depend on the direction of the applied exchange field. Moreover, the response is perfectly isotropic with respect to the rotation of the polarization of light in the plane. At the frequency of $\hbar\omega = 1.6$ eV, the spin density is suppressed for all three linear independent polarizations. Up to this frequency, the two in-plane and z-polarized signals have the same sign and frequency dependence, with the IP-polarized response being smaller in magnitude. At frequencies above $\hbar\omega = 2.0$ eV, the OOP response becomes negative while the IP responses remain positive. For example, at $\hbar\omega = 2.9$ eV, the spin density can be switched between the values of $\delta S_{\perp N}^{(a)} \approx \pm 10 \times 10^{-6} \frac{\hbar}{2}$ when rotating the linear polarization from within the xy-plane into the z-direction. The discussed chiral spin density can be seen as a result of the action of an exchange field on the staggered spin density generated along **N**, $\delta S_{\parallel N}^-$, which gets canted, resulting in an effective ferromagnetic moment and associated chiral spin density pointing along the exchange field. This spin density response can effectively drive a spin-polarized current via the spin galvanic effect.[80] Indeed, we observe a generation of colossal LPGE-like spin photocurrents that propagate along z with spin-polarization along $\mathbf{i} \times \mathbf{N}$ [see the lower part of Figs. 13(a) and 13(b)], with a magnitude that is larger by an order of magnitude as compared to collinear spin photocurrents, discussed earlier, reaching as much as 1760×10^{10} $[\hbar/(2e)$ A/m$^2]$ for light polarized along z at $\hbar\omega = 3.0$ eV. Interestingly, while the LPGE chiral photocurrents of charge are significantly suppressed for the IP canting (not shown), the chiral spin photocurrents are found to correlate directly with the chiral spin density, both in terms of frequency dependence and light polarization dependence, as well as in their "insensitivity" to the direction of the applied canting field. As the insets show, the chiral laser-induced spin density scales linearly with the applied exchange field up to the field strength of 200 meV, and we also confirm that the linear behavior in this range is preserved by other computed quantities. This implies that even at very small canting angles below one degree, the photo-induced chiral spin currents will be very large in overall magnitude and can serve as markers of both the effect of canting as well as its strength.

Besides the LPGE-like responses shown in Figs. 13(a) and 13(b), a helicity-switchable chiral CPGE-like photo-induced nonequilibrium spin density is induced along $\mathbf{i} \times \mathbf{N}$, accompanied by an associated spin-polarized photocurrent flowing along z with spins along **i**, as shown in Figs. 13(c) and 13(d). However, the predicted magnitude of the effects is two orders of magnitude smaller when compared to the LPGE-like responses, being overall comparable to the range of values for the collinear case. Here, we also do not observe any correlation in frequency dependence between the photo-induced spin density and the spin currents.

VII. CONCLUSIONS

In our work, using *ab initio* Keldysh formalism, we have scrutinized the response properties of Mn$_2$Au subjected to linearly and circularly polarized laser light. We explicitly computed the laser-induced photocurrents of charge and spin and the laser-induced spin-polarization. We found that the magnitude of the computed effects is sizable, and their nature is of purely magnetic origin. The extreme sensitivity of the effects to the sense of light polarization, the direction of the Néel vector, light frequency, and quasiparticle lifetime was observed. The diversity of observed responses suggests that the dynamical properties of staggered magnetization in this material can be detected by tracking the dynamics of the photocurrents. We have uncovered and studied the emergence of the photospin Hall effect in Mn$_2$Au, which governs the generation of transverse photocurrents of spin in response to generated charge photocurrents in this system. Finally, we predict that colossal chiral spin photocurrents can be generated even upon a very small canting of staggered moments, which suggests that antiferromagnetic dynamics accompanied by intrinsic reorganization of the magnetic order may find a prominent place in optospintronics applications as a strong source of optically generated spin currents.

AUTHOR DECLARATIONS

Conflict of Interest

The authors have no conflicts to disclose.

Author Contributions

M. Merte: Conceptualization (equal); Data curation (lead); Investigation (lead); Methodology (lead); Software (lead); Writing – original draft (equal); Writing – review & editing (equal). **F. Freimuth**: Investigation (supporting); Methodology (supporting); Software (supporting); Supervision (supporting); Writing – original draft (supporting); Writing – review & editing (supporting). **D. Go**: Methodology (supporting); Software (supporting); Writing – review & editing (supporting). **T. Adamantopoulos**: Methodology (supporting); Software (supporting); Writing – review & editing

01 August 2023 10:53:16

(supporting). **F. R. Lux**: Conceptualization (supporting); Methodology (supporting); Software (supporting); Writing – review & editing (supporting). **L. Plucinski**: Conceptualization (supporting); Supervision (supporting); Writing – original draft (supporting). **O. Gomonay**: Conceptualization (supporting); Methodology (supporting); Supervision (supporting); Writing – review & editing (supporting). **S. Blügel**: Conceptualization (supporting); Supervision (supporting); Writing – review & editing (supporting). **Y. Mokrousov**: Conceptualization (lead); Project administration (lead); Resources (lead); Supervision (lead); Writing – original draft (equal); Writing – review & editing (equal).

DATA AVAILABILITY

The data that support the findings of this study are available from the corresponding author upon reasonable request.

REFERENCES

[1] T. Jungwirth, X. Marti, P. Wadley, and J. Wunderlich, "Antiferromagnetic spintronics," Nat. Nanotechnol. **11**, 231–241 (2016).

[2] T. Jungwirth, J. Sinova, A. Manchon, X. Marti, J. Wunderlich, and C. Felser, "The multiple directions of antiferromagnetic spintronics," Nat. Phys. **14**, 200–203 (2018).

[3] W. A. Borders, H. Akima, S. Fukami, S. Moriya, S. Kurihara, Y. Horio, S. Sato, and H. Ohno, "Analogue spin–orbit torque device for artificial-neural-network-based associative memory operation," Appl. Phys. Express **10**, 013007 (2016).

[4] T. Kosub, M. Kopte, R. Hühne, P. Appel, B. Shields, P. Maletinsky, R. Hübner, M. O. Liedke, J. Fassbender, O. G. Schmidt, and D. Makarov, "Purely antiferromagnetic magnetoelectric random access memory," Nat. Commun. **8**, 13985 (2017).

[5] K. Olejník, T. Seifert, Z. Kašpar, V. Novák, P. Wadley, R. P. Campion, M. Baumgartner, P. Gambardella, P. Němec, J. Wunderlich, J. Sinova, P. Kužel, M. Müller, T. Kampfrath, and T. Jungwirth, "Terahertz electrical writing speed in an antiferromagnetic memory," Sci. Adv. **4**, eaar3566 (2018).

[6] K. Vahaplar, A. M. Kalashnikova, A. V. Kimel, D. Hinzke, U. Nowak, R. Chantrell, A. Tsukamoto, A. Itoh, A. Kirilyuk, and T. Rasing, "Ultrafast path for optical magnetization reversal via a strongly nonequilibrium state," Phys. Rev. Lett. **103**, 117201 (2009).

[7] M. Berritta, R. Mondal, K. Carva, and P. M. Oppeneer, "*Ab initio* theory of coherent laser-induced magnetization in metals," Phys. Rev. Lett. **117**, 137203 (2016).

[8] M. M. S. Barbeau, M. Titov, M. I. Katsnelson, and A. Qaiumzadeh, "Nonequilibrium magnons from hot electrons in antiferromagnetic systems," arXiv:2209.03469v1 (2022).

[9] T. Dannegger, M. Berritta, K. Carva, S. Selzer, U. Ritzmann, P. M. Oppeneer, and U. Nowak, "Ultrafast coherent all-optical switching of an antiferromagnet with the inverse Faraday effect," Phys. Rev. B **104**, L060413 (2021).

[10] P. Němec, M. Fiebig, T. Kampfrath, and A. Kimel, "Antiferromagnetic optospintronics," Nat. Phys. **14**, 229–241 (2018).

[11] T. Kampfrath, A. Sell, G. Klatt, A. Pashkin, S. Mährlein, T. Dekorsy, M. Wolf, M. Fiebig, A. Leitenstorfer, and R. Huber, "Coherent terahertz control of antiferromagnetic spin waves," Nat. Photonics **5**, 31–34 (2011).

[12] T. Janda, T. Ostatnicky, P. Nemec, E. Schmoranzerova, R. Campion, V. Hills, V. Novak, Z. Soban, and J. Wunderlich, "Ultrashort spin–orbit torque generated by femtosecond laser pulses," Sci. Rep. **12**, 21550 (2022).

[13] A. E. Fedianin, A. M. Kalashnikova, and J. H. Mentink, "Selection rules for ultrafast laser excitation and detection of spin correlations in a cubic antiferromagnet," arXiv:2212.14698 (2022).

[14] A. Farkas, K. Olejnik, M. Surynek, P. Nemec, V. Novak, and T. Jungwirth, "Optical control of magnetic configuration of an antiferromagnetic CuMnAs," in *Frontiers in Optics + Laser Science 2022 (FIO, LS)* (Optica Publishing Group, 2022), paper FW7C.3.

[15] Q. Ma, R. K. Kumar, S.-Y. Xu, F. H. L. Koppens, and J. C. W. Song, "Photocurrent as a multi-physics diagnostic of quantum materials," Nat. Rev. Phys. **5**, 170 (2022).

[16] D. Hamara, G. F. Lange, F. N. Kholid, A. Markou, C. Felser, R.-J. Slager, and C. Ciccarelli, "Helicity-dependent ultrafast photocurrents in Weyl magnet Mn$_3$Sn," arXiv:2302.07286 (2023).

[17] J. Železný, H. Gao, K. Výborný, J. Zemen, J. Mašek, A. Manchon, J. Wunderlich, J. Sinova, and T. Jungwirth, "Relativistic Néel-order fields induced by electrical current in antiferromagnets," Phys. Rev. Lett. **113**, 157201 (2014).

[18] S. Y. Bodnar, L. Šmejkal, I. Turek, T. Jungwirth, O. Gomonay, J. Sinova, A. A. Sapozhnik, H.-J. Elmers, M. Kläui, and M. Jourdan, "Writing and reading antiferromagnetic Mn$_2$Au by Néel spin-orbit torques and large anisotropic magnetoresistance," Nat. Commun. **9**, 348 (2018).

[19] M. Meinert, D. Graulich, and T. Matalla-Wagner, "Electrical switching of antiferromagnetic Mn$_2$Au and the role of thermal activation," Phys. Rev. Appl. **9**, 064040 (2018).

[20] V. Grigorev, M. Filianina, S. Y. Bodnar, S. Sobolev, N. Bhattacharjee, S. Bommanaboyena, Y. Lytvynenko, Y. Skourski, D. Fuchs, M. Kläui, M. Jourdan, and J. Demsar, "Optical readout of the Néel vector in the metallic antiferromagnet Mn$_2$Au," Phys. Rev. Appl. **16**, 014037 (2021).

[21] V. Grigorev, M. Filianina, Y. Lytvynenko, S. Sobolev, A. R. Pokharel, A. P. Lanz, A. Sapozhnik, A. Kleibert, S. Bodnar, P. Grigorev *et al.*, "Optically triggered Néel vector manipulation of a metallic antiferromagnet Mn$_2$Au under strain," ACS Nano **16**, 20589–20597 (2022).

[22] H. Watanabe and Y. Yanase, "Nonlinear electric transport in odd-parity magnetic multipole systems: Application to Mn-based compounds," Phys. Rev. Res. **2**, 043081 (2020).

[23] P. Wells and J. H. Smith, "The structure of Mn$_2$Au and Mn$_3$Au," Acta Crystallogr., Sect. A: Found. Adv. **26**, 379–381 (1970).

[24] S. Khmelevskyi and P. Mohn, "Layered antiferromagnetism with high Neel temperature in the intermetallic compound Mn$_2$Au," Appl. Phys. Lett. **93**, 162503 (2008).

[25] See www.flapw.de for the details of the method and its implementation.

[26] J. P. Perdew, K. Burke, and M. Ernzerhof, "Generalized gradient approximation made simple," Phys. Rev. Lett. **77**, 3865–3868 (1996).

[27] G. Pizzi, V. Vitale, R. Arita, S. Blügel, F. Freimuth, G. Géranton, M. Gibertini, D. Gresch, C. Johnson, T. Koretsune, J. Ibañez-Azpiroz, H. Lee, J.-M. Lihm, D. Marchand, A. Marrazzo, Y. Mokrousov, J. I. Mustafa, Y. Nohara, Y. Nomura, L. Paulatto, S. Poncé, T. Ponweiser, J. Qiao, F. Thöle, S. S. Tsirkin, M. Wierzbowska, N. Marzari, D. Vanderbilt, I. Souza, A. A. Mostofi, and J. R. Yates, "Wannier90 as a community code: New features and applications," J. Phys.: Condens. Matter **32**, 165902 (2020).

[28] J. P. van der Ziel, P. S. Pershan, and L. D. Malmstrom, "Optically-induced magnetization resulting from the inverse Faraday effect," Phys. Rev. Lett. **15**, 190–193 (1965).

[29] K. Taguchi and G. Tatara, "Theory of inverse Faraday effect in a disordered metal in the terahertz regime," Phys. Rev. B **84**, 174433 (2011).

[30] F. Freimuth, S. Blügel, and Y. Mokrousov, "Laser-induced torques in metallic ferromagnets," Phys. Rev. B **94**, 144432 (2016).

[31] F. Freimuth, S. Blügel, and Y. Mokrousov, "Charge and spin photocurrents in the Rashba model," Phys. Rev. B **103**, 075428 (2021).

[32] M. Merte, F. Freimuth, T. Adamantopoulos, D. Go, T. G. Saunderson, M. Kläui, L. Plucinski, O. Gomonay, S. Blügel, and Y. Mokrousov, "Photocurrents of charge and spin in monolayer Fe$_3$GeTe$_2$," Phys. Rev. B **104**, L220405 (2021).

[33] T. Adamantopoulos, M. Merte, D. Go, F. Freimuth, S. Blügel, and Y. Mokrousov, "Laser-induced charge and spin photocurrents at the BiAg$_2$ surface: A first-principles benchmark," Phys. Rev. Res. **4**, 043046 (2022).

[34] V. I. Belinicher and B. I. Sturman, "The photogalvanic effect in media lacking a center of symmetry," Usp. Fiz. Nauk **130**, 415–458 (1980).

[35] W. Kraut and R. von Baltz, "Anomalous bulk photovoltaic effect in ferroelectrics: A quadratic response theory," Phys. Rev. B **19**, 1548–1554 (1979).

[36] J. E. Sipe and A. I. Shkrebtii, "Second-order optical response in semiconductors," Phys. Rev. B **61**, 5337–5352 (2000).

[37] J. Ibañez-Azpiroz, S. S. Tsirkin, and I. Souza, "*Ab initio* calculation of the shift photocurrent by Wannier interpolation," Phys. Rev. B **97**, 245143 (2018).

[38] J. Rammer and H. Smith, "Quantum field-theoretical methods in transport theory of metals," Rev. Mod. Phys. **58**, 323–359 (1986).

[39] F. Freimuth, S. Blügel, and Y. Mokrousov, "Laser-induced currents of charge and spin in the Rashba model," arXiv:1710.10480 [cond-mat.mes-hall] (2017).

[40] T. J. Huisman, R. V. Mikhaylovskiy, J. D. Costa, F. Freimuth, E. Paz, J. Ventura, P. P. Freitas, S. Blügel, Y. Mokrousov, T. Rasing, and A. V. Kimel, "Femtosecond control of electric currents in metallic ferromagnetic heterostructures," Nat. Nanotechnol. **11**, 455–458 (2016).

[41] L. Kadanoff and G. Baym, *Quantum Statistical Mechanics: Green's Function Methods in Equilibrium and Nonequilibrium Problems* (CRC Press, Boca Raton, 1962).

[42] F. Freimuth, S. Blügel, and Y. Mokrousov, "Laser-induced torques in metallic antiferromagnets," Phys. Rev. B **103**, 174429 (2021).

[43] D.-F. Shao, S.-H. Zhang, G. Gurung, W. Yang, and E. Y. Tsymbal, "Nonlinear anomalous Hall effect for Néel vector detection," Phys. Rev. Lett. **124**, 067203 (2020).

[44] V. M. T. S. Barthem, C. V. Colin, R. Haettel, D. Dufeu, and D. Givord, "Easy moment direction and antiferromagnetic domain wall motion in Mn_2Au," J. Magn. Magn. Mater. **406**, 289–292 (2016).

[45] Y. Zhang, H. Ishizuka, J. van den Brink, C. Felser, B. Yan, and N. Nagaosa, "Photogalvanic effect in Weyl semimetals from first principles," Phys. Rev. B **97**, 241118 (2018).

[46] Y. Zhang, T. Holder, H. Ishizuka, F. de Juan, N. Nagaosa, C. Felser, and B. Yan, "Switchable magnetic bulk photovoltaic effect in the two-dimensional magnet CrI_3," Nat. Commun. **10**, 3783 (2019).

[47] T. Holder, D. Kaplan, R. Ilan, and B. Yan, "Mixed axial-gravitational anomaly from emergent curved spacetime in nonlinear charge transport," Nature Communications **14**, 3053 (2023).

[48] D. Kaplan, T. Holder, and B. Yan, "Unification of nonlinear anomalous Hall effect and nonreciprocal magnetoresistance in metals by the quantum geometry," arXiv:2211.17213 [cond-mat.mes-hall] (2022).

[49] J. Ahn, G.-Y. Guo, N. Nagaosa, and A. Vishwanath, "Riemannian geometry of resonant optical responses," Nat. Phys. **18**, 290–295 (2022).

[50] H. Wang and X. Qian, "Electrically and magnetically switchable nonlinear photocurrent in PT-symmetric magnetic topological quantum materials," Npj Comput. Mater. **6**, 199 (2020).

[51] P. Wadley, B. Howells, J. Zelezny, C. Andrews, V. Hills, R. P. Campion, V. Novak, F. Freimuth, Y. Mokrousov, A. W. Rushforth, K. W. Edmonds, B. L. Gallagher, and T. Jungwirth, "Electrical switching of an antiferromagnet," Science **351**, 587 (2015).

[52] Q. Shao, P. Li, L. Liu, H. Yang, S. Fukami, A. Razavi, H. Wu, K. Wang, F. Freimuth, Y. Mokrousov, M. D. Stiles, S. Emori, A. Hoffmann, J. Åkerman, K. Roy, J.-P. Wang, S.-H. Yang, K. Garello, and W. Zhang, "Roadmap of spin–orbit torques," IEEE Trans. Magn. **57**, 800439 (2021).

[53] M. Weißenhofer, F. Foggetti, U. Nowak, and P. M. Oppeneer, "Néel-vector switching and terahertz spin-wave excitation in Mn_2Au due to femtosecond spin-transfer torques," Phys. Rev. B **107**, 174424 (2023).

[54] J. Wunderlich, B. Kaestner, J. Sinova, and T. Jungwirth, "Experimental observation of the spin-Hall effect in a two-dimensional spin-orbit coupled semiconductor system," Phys. Rev. Lett. **94**, 047204 (2005).

[55] V. Sih, W. H. Lau, R. C. Myers, V. R. Horowitz, A. C. Gossard, and D. D. Awschalom, "Generating spin currents in semiconductors with the spin Hall effect," Phys. Rev. Lett. **97**, 096605 (2006).

[56] J. Wätzel and J. Berakdar, "All-optical generation and ultrafast tuning of nonlinear spin Hall current," Sci. Rep. **8**, 17102 (2018).

[57] S. Hayami, M. Yatsushiro, and H. Kusunose, "Nonlinear spin Hall effect in PT-symmetric collinear magnets," Phys. Rev. B **106**, 024405 (2022).

[58] R. Fei, W. Song, L. Pusey-Nazzaro, and L. Yang, "*PT*-symmetry-enabled spin circular photogalvanic effect in antiferromagnetic insulators," Phys. Rev. Lett. **127**, 207402 (2021).

[59] R.-C. Xiao, D.-F. Shao, Y.-H. Li, and H. Jiang, "Spin photogalvanic effect in two-dimensional collinear antiferromagnets," npj Quantum Mater. **6**, 35 (2021).

[60] H. Xu, H. Wang, J. Zhou, and J. Li, "Pure spin photocurrent in non-centrosymmetric crystals: Bulk spin photovoltaic effect," Nat. Commun. **12**, 4330 (2021).

[61] T. Kimura, Y. Otani, T. Sato, S. Takahashi, and S. Maekawa, "Room-temperature reversible spin Hall effect," Phys. Rev. Lett. **98**, 156601 (2007).

[62] L. Liu, T. Moriyama, D. C. Ralph, and R. A. Buhrman, "Spin-torque ferromagnetic resonance induced by the spin Hall effect," Phys. Rev. Lett. **106**, 036601 (2011).

[63] L. Liu, O. J. Lee, T. J. Gudmundsen, D. C. Ralph, and R. A. Buhrman, "Current-induced switching of perpendicularly magnetized magnetic layers using spin torque from the spin Hall effect," Phys. Rev. Lett. **109**, 096602 (2012).

[64] W. Chen, M. Sigrist, J. Sinova, and D. Manske, "Minimal model of spin-transfer torque and spin pumping caused by the spin Hall effect," Phys. Rev. Lett. **115**, 217203 (2015).

[65] V. P. Amin and M. D. Stiles, "Spin transport at interfaces with spin-orbit coupling: Formalism," Phys. Rev. B **94**, 104419 (2016).

[66] A. Manchon, J. Železný, I. M. Miron, T. Jungwirth, J. Sinova, A. Thiaville, K. Garello, and P. Gambardella, "Current-induced spin-orbit torques in ferromagnetic and antiferromagnetic systems," Rev. Mod. Phys. **91**, 035004 (2019).

[67] T. Kampfrath, M. Battiato, P. Maldonado, G. Eilers, J. Nötzold, S. Mährlein, V. Zbarsky, F. Freimuth, Y. Mokrousov, S. Blügel, M. Wolf, I. Radu, P. M. Oppeneer, and M. Münzenberg, "Terahertz spin current pulses controlled by magnetic heterostructures," Nat. Nanotechnol. **8**, 256–260 (2013).

[68] T. Seifert, S. Jaiswal, U. Martens, J. Hannegan, L. Braun, P. Maldonado, F. Freimuth, A. Kronenberg, J. Henrizi, I. Radu, E. Beaurepaire, Y. Mokrousov, P. M. Oppeneer, M. Jourdan, G. Jakob, D. Turchinovich, L. M. Hayden, M. Wolf, M. Münzenberg, M. Kläui, and T. Kampfrath, "Efficient metallic spintronic emitters of ultrabroadband terahertz radiation," Nat. Photonics **10**, 483–488 (2016).

[69] F. Freimuth, S. Blügel, and Y. Mokrousov, "Anisotropic spin Hall effect from first principles," Phys. Rev. Lett. **105**, 246602 (2010).

[70] K. Shen, G. Vignale, and R. Raimondi, "Microscopic theory of the inverse Edelstein effect," Phys. Rev. Lett. **112**, 096601 (2014).

[71] F. Freimuth, S. Blügel, and Y. Mokrousov, "Charge pumping driven by the laser-induced dynamics of the exchange splitting," Phys. Rev. B **95**, 094434 (2017).

[72] L. Šmejkal, R. González-Hernández, T. Jungwirth, and J. Sinova, "Crystal time-reversal symmetry breaking and spontaneous Hall effect in collinear antiferromagnets," Sci. Adv. **6**, eaaz8809 (2020).

[73] Z. Feng, X. Zhou, L. Šmejkal, L. Wu, Z. Zhu, H. Guo, R. González-Hernández, X. Wang, H. Yan, P. Qin, X. Zhang, H. Wu, H. Chen, Z. Xia, C. Jiang, M. Coey, J. Sinova, T. Jungwirth, and Z. Liu, "Observation of the anomalous Hall effect in a collinear antiferromagnet," Nature Electronics **5**, 735–743 (2022).

[74] J. Kipp, K. Samanta, F. R. Lux, M. Merte, D. Go, J.-P. Hanke, M. Redies, F. Freimuth, S. Blügel, M. Ležaić et al., "The chiral Hall effect in canted ferromagnets and antiferromagnets," Commun. Phys. **4**, 99 (2021).

[75] S.-K. Bac, K. Koller, F. Lux, J. Wang, L. Riney, K. Borisiak, W. Powers, M. Zhukovskyi, T. Orlova, M. Dobrowolska et al., "Topological response of the anomalous Hall effect in $MnBi_2Te_4$ due to magnetic canting," npj Quantum Mater. **7**, 46 (2022).

[76] M. Kimata, H. Chen, K. Kondou, S. Sugimoto, P. K. Muduli, M. Ikhlas, Y. Omori, T. Tomita, A. H. MacDonald, S. Nakatsuji, and Y. Otani, "Magnetic and magnetic inverse spin Hall effects in a non-collinear antiferromagnet," Nature **565**, 627–630 (2019).

[77] T. Nan, C. X. Quintela, J. Irwin, G. Gurung, D.-F. Shao, J. Gibbons, N. Campbell, K. Song, S.-Y. Choi, L. Guo et al., "Controlling spin current polarization through non-collinear antiferromagnetism," Nat. Commun. **11**, 4671 (2020).

[78] H. Masuda, T. Seki, J.-i. Ohe, Y. Nii, K. Takanashi, and Y. Onose, "Chirality-dependent spin current generation in a helimagnet: Zero-field probe of chirality," arXiv:2212.10980 (2022).

[79] D. Go, M. Sallermann, F. R. Lux, S. Blügel, O. Gomonay, and Y. Mokrousov, "Noncollinear spin current for switching of chiral magnetic textures," Phys. Rev. Lett. **129**, 097204 (2022).

[80] S. D. Ganichev, E. L. Ivchenko, V. V. Bel'kov, S. A. Tarasenko, M. Sollinger, D. Weiss, W. Wegscheider, and W. Prettl, "Spin-galvanic effect," Nature **417**, 153–156 (2002).